

# Assessing sub-grid variability within satellite pixels over urban regions using airborne mapping spectrometer measurements

Wenfu Tang<sup>1,2</sup>, David P. Edwards<sup>2</sup>, Louisa K. Emmons<sup>2</sup>, Helen M. Worden<sup>2</sup>, Laura M. Judd<sup>3</sup>, Lok N. Lamsal<sup>4,5</sup>, Jassim A. Al-Saadi<sup>3</sup>, Scott J. Janz<sup>4</sup>, James H. Crawford<sup>3</sup>, Merritt N. Deeter<sup>2</sup>, Gabriele Pfister<sup>2</sup>, Rebecca R. Buchholz<sup>2</sup>, Benjamin Gaubert<sup>2</sup>, Caroline R. Nowlan<sup>6</sup>

<sup>1</sup>Advanced Study Program, National Center for Atmospheric Research, Boulder, CO, USA

<sup>2</sup>Atmospheric Chemistry Observations and Modeling, National Center for Atmospheric Research, Boulder, CO, USA

<sup>3</sup>NASA Langley Research Center, Hampton, VA 23681, USA

<sup>4</sup>NASA Goddard Space Flight Center, Greenbelt, MD 20771, USA

<sup>5</sup>Universities Space Research Association, Columbia, MD 21046, USA

<sup>6</sup>Harvard-Smithsonian Center for Astrophysics, Cambridge, MA 02138, USA

## Abstract

Sub-grid variability (SGV) of atmospheric trace gases within satellite pixels is a key issue in satellite design and interpretation and validation of retrieval products. However, characterizing this variability is challenging due to the lack of independent high-resolution measurements. Here we use tropospheric NO<sub>2</sub> vertical column (VC) measurements from the Geostationary Trace gas and Aerosol Sensor Optimization (GeoTASO) airborne instrument with a spatial resolution of about 250 m × 250 m to quantify the normalized SGV (i.e., the standard deviation of the sub-grid GeoTASO values within the sampled satellite pixel divided by the mean of the sub-grid GeoTASO values within the same satellite pixel) for different hypothetical satellite pixel sizes over urban regions. We use the GeoTASO measurements over the Seoul Metropolitan Area (SMA) and Busan region of South Korea during the 2016 KORUS-AQ field campaign, and over the Los Angeles Basin, USA, during the 2017 SARP field campaign. We find that the normalized SGV of NO<sub>2</sub> VC increases with increasing satellite pixel sizes (from ~10% for 0.5 km × 0.5 km pixel size to ~35% for 25 km × 25 km pixel size), and this relationship holds for the three study regions, which are also within the domains of upcoming geostationary satellite air quality missions. We also quantify the temporal variability of the retrieved NO<sub>2</sub> VC within the same hypothetical satellite pixels (represented by the difference of retrieved values at two or more different times in a day). For a given satellite pixel size, the temporal variability within the same satellite pixels increases with the sampling time difference over SMA. For a given small (e.g., <=4 hours) sampling time difference within the same satellite pixels, the temporal variability of the retrieved NO<sub>2</sub> VC increases with the increasing spatial resolution over the SMA, Busan region, and the Los Angeles basin.

Deleted: ,

Deleted: their

Deleted: sampled

Deleted: of

42 The results of this study have implications for future satellite design and retrieval  
43 interpretation, and validation when comparing pixel data with local observations. In addition, the  
44 analyses presented in this study are equally applicable in model evaluation when comparing model  
45 grid values to local observations. Results from the Weather Research and Forecasting model  
46 coupled with Chemistry (WRF-Chem) model indicate that the normalized satellite SGV of  
47 tropospheric NO<sub>2</sub> VC calculated in this study could serve as an upper bound to the satellite SGV  
48 of other species (e.g., CO and SO<sub>2</sub>) that share common source(s) with NO<sub>2</sub> but have relatively  
49 longer lifetime.  
50

## 51 1. Introduction

52 Characterizing sub-grid variability (SGV) of atmospheric chemical constituent fields is  
53 important in both satellite retrievals and atmospheric chemical-transport modeling. This is  
54 especially the case over urban regions where strong variability and heterogeneity exist. The  
55 inability to resolve sub-grid details is one of the fundamental limitations of grid-based models  
56 (Qian et al., 2010) and has been studied extensively (e.g., Boersma et al., 2016; Ching et al., 2006;  
57 Denby et al., 2011; Pillai et al., 2010; Qian et al., 2010). Pillai et al. (2010) found that the SGV of  
58 column-averaged carbon dioxide (CO<sub>2</sub>) can reach up to 1.2 ppm in global models that have a  
59 horizontal resolution of 100 km. This is an order of magnitude larger than sampling errors that  
60 include both limitations in instrument precision and uncertainty of unresolved atmospheric CO<sub>2</sub>  
61 variability within the mixed layer (Gerbig et al., 2003). Denby et al. (2011) suggested that the  
62 average European urban background exposure for nitrogen dioxide (NO<sub>2</sub>) using a model of 50-km  
63 resolution is underestimated by ~44% due to SGV.

64 In contrast, much less attention has been paid to the sub-grid variability within satellite  
65 pixels (e.g., Broccardo et al., 2018; Judd et al., 2019; Tack et al., 2020). Indeed, some previous  
66 studies (e.g., Kim et al., 2016; Song et al., 2018; Zhang et al., 2019; Choi et al., 2020) used satellite  
67 retrievals to study SGV in models, and calculated representativeness errors of model results with  
68 respect to the satellite measurements (e.g., Pillai et al., 2010). Even though satellite retrievals of  
69 atmospheric composition often have smaller uncertainties than model results, it has not been until  
70 recently that the typical spatial resolution of atmospheric composition satellite products has  
71 reached scales comparable to regional atmospheric chemistry models (<~10 km).

72 Quantification of satellite SGV has historically been limited by insufficient spatial  
73 coverage of in situ measurements, and is a key issue in designing, understanding, validating and  
74 correctly interpreting satellite observations. This is especially important in the satellite instrument  
75 development process, during which the required measurement precision and retrieval resolution  
76 need to be defined in order to meet the mission science goals. In addition, when validating and  
77 evaluating relatively coarse-scale satellite retrievals by comparing with surface in situ observations,  
78 SGV introduces large uncertainties on top of the existing uncertainty introduced by imperfect  
79 knowledge of the trace gas vertical profiles. Accurate quantification of satellite SGV can therefore  
80 facilitate the estimate of sampling uncertainty for satellite product validation/evaluation. Temporal  
81 variability within sampled satellite pixels is also an important issue in satellite design, validation,  
82 and application. For polar-orbiting satellites, knowledge of temporal variability is necessary to  
83 analyze the representativeness of satellite retrievals at specific overpass times. For geostationary  
84 Earth orbit (GEO) satellites, developing a measure of the temporal variability of fine-scale spatial

Deleted: .

Deleted: Until recently, accurate in-situ measurements with sufficient spatiotemporal coverage . As a result, it has been challenging to quantify satellite SGV, even though this is

Deleted: , validating

Deleted: ,

Deleted: surface

Deleted: .

93 structure will be important for assessing coincidence during validation of the new hourly  
 94 observations. This work is partly motivated by validation requirements and considerations for the  
 95 upcoming GEO satellite constellation for atmospheric composition that includes the Tropospheric  
 96 Emissions: Monitoring Pollution (TEMPO) mission over North America (Chance et al., 2013;  
 97 Zoogman et al., 2017), the Geostationary Environment Monitoring Spectrometer (GEMS) over  
 98 Asia (Kim et al., 2020), and the Sentinel-4 mission over Europe (Courrèges-Lacoste et al., 2017).

Deleted: geostationary orbit (

Deleted: )

99 Airborne mapping spectrometer measurements provide dense observations within the  
 100 several-kilometer footprint of a typical satellite pixel. This feature of airborne mapping  
 101 spectrometer measurements provides a unique opportunity to estimate satellite SGV in addition to  
 102 their role in satellite validation. For example, Broccardo et al. (2018) used aircraft measurements  
 103 of NO<sub>2</sub> from an imaging differential optical absorption spectrometer (iDOAS) instrument to study  
 104 intra-pixel variability in satellite tropospheric NO<sub>2</sub> column over South Africa, whilst Judd et al.  
 105 (2019) evaluated the impact of spatial resolution on tropospheric NO<sub>2</sub> column comparisons with  
 106 in situ observations using the NO<sub>2</sub> measurements of the Geostationary Trace gas and Aerosol  
 107 Sensor Optimization (GeoTASO). GeoTASO is an airborne remote sensing instrument capable of  
 108 high spatial resolution retrieval of UV-VIS absorbing species such as NO<sub>2</sub> and formaldehyde  
 109 (HCHO; Nowlan et al., 2018) and sulfur dioxide (SO<sub>2</sub>; Chong et al., 2020), and has measurement  
 110 characteristics similar to the GEMS and TEMPO GEO satellite instruments. The GeoTASO data  
 111 used here were taken in gapless, grid-like patterns – or “rasters” – over the regions of interest,  
 112 providing essentially continuous spatial coverage that was repeated during multiple flights up to  
 113 four times a day in some cases. As such, the GeoTASO data (with a spatial resolution of ~250 m  
 114 × 250 m) provide a preview of the type of sampling that is expected from the GEO satellite sensors,  
 115 making the data particularly suitable for our study. We focus on the GeoTASO measurements  
 116 made during the Korea United States Air Quality (KORUS-AQ) field experiment in 2016  
 117 (Crawford et al., 2021). The measurements from KORUS-AQ have been widely used by  
 118 researchers for various air quality topics, including quantification of emissions and model and  
 119 satellite evaluation (e.g., Deeter et al., 2019; Huang et al., 2018; Kim et al., 2018; Miyazaki et al.,  
 120 2019; Spinei et al., 2018; Tang et al., 2018, 2019; Souri et al., 2020; Gaubert et al., 2020). We  
 121 further compare our findings from KORUS-AQ with flights conducted during the NASA Student  
 122 Airborne Research Program (SARP) in 2017 over the Los Angeles (LA) Basin to test the general  
 123 applicability of our findings over a different urban region. The KORUS-AQ mission took place  
 124 within the GEMS domain, while the SARP in 2017 is within the domain of TEMPO. Given the  
 125 similarity between the TEMPO and GEMS instruments in terms of spectral ranges, spectral and  
 126 spatial resolution, and retrieval algorithms (Al-Saadi et al., 2014), such comparison is reasonable  
 127 and useful in facilitating the generalization of the results from the study.

Deleted: several-kilometers footprinttypical , whilst

Deleted: The measurements of the Geostationary Trace gas and Aerosol Sensor Optimization (

Deleted: )

Deleted: airborne instrument provide a unique dataset for quantifying satellite SGV. GeoTASO

Deleted: like

Deleted: ,

Deleted: with

128 We use the tropospheric NO<sub>2</sub> vertical column (VC) retrieved by GeoTASO as a tool to  
 129 assess satellite SGV and temporal variability for different hypothetical satellite pixel sizes over  
 130 urban regions. Because spatial SGV and temporal variability both vary with satellite pixel size, the  
 131 two need to be considered together to enhance the accuracy of satellite product analyses. NO<sub>2</sub> is  
 132 an important air pollutant that is primarily generated from anthropogenic sources such as emissions  
 133 from the energy, transportation, and industry sectors (Hoesly et al., 2018). It is a reactive gas with  
 134 a typical lifetime of a few hours in the planetary boundary layer (PBL), although it can also be  
 135 transported over long distance in the form of peroxyacetyl nitrate (PAN) and nitric acid. NO<sub>2</sub> is a  
 136 precursor of tropospheric ozone and secondary aerosols and has a negative impact on human health

Deleted: NO<sub>2</sub>

Deleted: ,

150 and the environment (Finlayson-Pitts et al., 1997). The results from this paper’s analysis of NO<sub>2</sub>  
151 also have implications for other air pollutants that share common source(s) with NO<sub>2</sub>, but that have  
152 somewhat longer lifetimes, for example, carbon monoxide (CO) and SO<sub>2</sub>.

153 In this study, we apply a satellite pixel random sampling technique and the spatial structure  
154 function analysis to GeoTASO data (described in Section 2) to quantify the SGV of satellite pixel  
155 NO<sub>2</sub> VC over three urban regions at a variety of spatial resolutions. We analyze the relationship  
156 between satellite pixel size and satellite SGV, and the relationship between satellite pixel size and  
157 the temporal variability of NO<sub>2</sub> observations (Section 3). We then discuss the implications for  
158 satellite design, satellite retrieval interpretation, satellite validation and evaluation, and satellite–  
159 in situ data comparisons (Section 4). Implications for general local observations and grid data  
160 comparisons are also discussed. Section 5 presents our conclusions.

161 **2. Data and methods**

162 In this section, we describe the GeoTASO instrument, campaign flights and the different  
163 analysis techniques used to characterize the satellite pixel SGV. We outline two approaches:  
164 satellite pixel random sampling to investigate separately both spatial variability and temporal  
165 variability, and the construction of spatial structure functions for an alternative measure of spatial  
166 variability.

167 **2.1 GeoTASO instrument**

168 In this study, we focus on GeoTASO retrievals of tropospheric NO<sub>2</sub> VC. GeoTASO is a  
169 hyperspectral instrument (Leitch et al., 2014) that measures nadir backscattered light in the  
170 ultraviolet (UV; 290–400 nm) and visible (VIS; 415–695 nm). As one of NASA’s airborne UV–  
171 VIS mapping instruments, it was designed to support the upcoming GEO satellite missions by  
172 acquiring high temporal and spatial resolution measurements with dense sampling for optimizing  
173 and experimenting with new retrieval algorithms (Leitch et al., 2014; Nowlan et al., 2016; Lamsal  
174 et al., 2017; Judd et al., 2019).

175 NO<sub>2</sub> is retrieved from GeoTASO spectra using the Differential Optical Absorption  
176 Spectroscopy (DOAS) technique. The retrieval methods and Level 2 data processing are described  
177 in Lamsal et al. (2017) and Souri et al. (2020) for KORUS-AQ and in Judd et al. (2019) for SARP.  
178 Although beyond the scope of this work, it is important to recognize that assumptions made in the  
179 retrieval process (e.g., assumed vertical distribution of the NO<sub>2</sub> profile) could affect the final  
180 variability of the retrieved NO<sub>2</sub> fields. GeoTASO has a cross-track field of view of 45° (+/- 22.5°  
181 from nadir), and the retrieval pixel size is approximately 250 m×250 m from typical flight altitudes  
182 of 24,000–28,000 feet (7.3–8.5 km). The dense sampling of airborne remote sensing measurements  
183 such as GeoTASO is a unique feature that provides the opportunity to study the expected spatial  
184 and temporal variability within satellite retrieved NO<sub>2</sub> pixels at high resolution. We use cloud-free  
185 GeoTASO data in this study. GeoTASO NO<sub>2</sub> VC retrievals have been validated with aircraft in  
186 situ data and ground-based Pandora remote sensing measurements during KORUS-AQ. Validation  
187 of GeoTASO NO<sub>2</sub> VC retrievals with aircraft in situ data suggested ~25% average difference,  
188 while agreement with Pandora is better with a difference of ~10% on average. Mean difference  
189 between Pandora and aircraft in situ data is ~20%. These validation results of GeoTASO NO<sub>2</sub> VC

Deleted: Vertical Column (  
Deleted: )

Formatted: Subscript  
Deleted: at nadir  
Deleted: The dense sampling of the GeoTASO datasets  
Deleted: and  
Deleted: the  
Deleted: retrieval  
Deleted: The  
Deleted: used  
Deleted: are mostly cloud-free  
Formatted: Font color: Text 1  
Deleted: se  
Deleted: are

202 retrievals are better than that reported by Nowlan et al. (2016). GeoTASO NO<sub>2</sub> VC retrievals  
203 during 2017 SARP have also been validated with Pandora data (Judd et al., 2019).

Deleted: Validation of GeoTASO NO<sub>2</sub> retrievals during KORUS-AQ with Pandora shows ~10% difference on average. The uncertainty estimate is lower than that reported by Nowlan et al. [2016].

## 204 2.2 The 2016 KORUS-AQ field campaign

Deleted: Al-Saadi et al., 2014

205 The KORUS-AQ field measurement campaign (Crawford et al., 2021), took place in May–  
206 June 2016, to help understand the factors controlling air quality over South Korea. One of the goals  
207 of KORUS-AQ was the testing and improvement of remote sensing algorithms in advance of the  
208 launches of the GEMS, TEMPO, and Sentinel-4 satellite missions. It is hoped that the high-quality  
209 initial data products from the GEO missions will facilitate their rapid uptake in air quality  
210 applications after launch (Al-Saadi et al., 2014; Kim et al., 2020). During KORUS-AQ, GeoTASO  
211 flew onboard the NASA LaRC B200 aircraft. We focus on the data taken over the Seoul  
212 Metropolitan Area (SMA) that is highly urbanized and polluted, and the greater Busan region that  
213 is less urbanized and less polluted than SMA (Figure 1). Figure 2 shows the 12 GeoTASO data  
214 rasters (i.e., gapless maps) acquired over SMA. It took ~4 hours to sample the large-area rasters  
215 (i.e., 0511AM, 0517AM, 0517PM, 0528PM), and ~2 hours to sample small-area rasters (i.e.,  
216 0601PM, 0602AM, 0605AM, 0609AM, and 0609PM). Figure S1 shows the 2 GeoTASO rasters  
217 acquired over the Busan region.

Deleted: ,

Deleted: somewhat

## 218 2.3 The 2017 SARP field campaign

219 During the NASA Student Airborne Research Program (SARP) flights in June 2017,  
220 (https://airbornescience.nasa.gov/content/Student\_Airborne\_Research\_Program), GeoTASO was  
221 flown onboard the NASA LaRC UC-12B aircraft over the LA Basin (Figure S2, which also shows  
222 the landcover). A detailed description and analysis of these data can be found in Judd et al. (2018;  
223 2019). In this study, we compare our analyses of the KORUS-AQ GeoTASO data with that from  
224 SARP over the LA Basin to test the general applicability of our findings.

Deleted: and findings from

Deleted: those using the GeoTASO data

## 225 2.4 Satellite pixel random sampling for spatial variability

226 The sampling strategy with GeoTASO provides a raster of continuous measurements in a  
227 mapped gapless pattern at high spatial resolution (Figures 2, S1, and S2). This dataset allows us to  
228 sample and study the SGV of coarser spatial resolution hypothetical satellite pixels sampling the  
229 same domain. To mimic satellite observations and quantify the satellite SGV, we randomly sample  
230 the GeoTASO data with hypothetical satellite pixels spanning 27 different pixel sizes (0.5 km×0.5  
231 km, 0.75 km×0.75 km, 1 km×1 km, 2 km×2 km, up to 25 km×25 km). Because of the transition to  
232 better spatial resolution for the future satellite missions, and the coverage limitation in the  
233 maximum hypothetical satellite pixel size sampled using the random sampling method, the  
234 analysis of SGV only goes up to 25 km × 25 km. This sampling process is conducted for each hour  
235 of each selected flight over the regions of interest during the KORUS-AQ and SARP campaigns.  
236 For every sampled satellite pixel, the mean (MEAN<sub>pixel</sub>) and standard deviation (SD<sub>pixel</sub>) of the  
237 GeoTASO tropospheric NO<sub>2</sub> VC data within the pixel are calculated to represent the satellite SGV.  
238 Normalized satellite SGV is calculated as the standard deviation of the GeoTASO data within the  
239 sampled satellite pixel divided by the mean of the GeoTASO data within the same sampled satellite  
240 pixel (SD<sub>pixel</sub>/MEAN<sub>pixel</sub>).

Deleted: map

Deleted: move to smaller pixel sizes in

Deleted: by

We use a set of 10,000 hypothetical satellite pixels at each size to include all of the GeoTASO data in the analysis and to cover as many locations as possible. Because the data are located closely in space but may be sampled at slightly different times for the same flight, we separate GeoTASO data into hourly bins for each flight before pixel sampling in order to reduce the impact of temporal variability of the GeoTASO data within a single satellite pixel sample.

Moved down [3]: Our sensitivity test indicates that the results do not change by halving the sample size.

As an illustration, we describe the procedure below for the May 17<sup>th</sup> afternoon flight (Figure 3) that was conducted from 13:00 to 17:00 local time: (1) the GeoTASO data during this flight were divided into four hourly groups according to the measurement time, i.e., 13:00-14:00, 14:00-15:00, 15:00-16:00, and 16:00-17:00; (2) for each of the 27 hypothetical satellite pixel sizes, we randomly generate 10,000 satellite pixel locations within each hourly group. Therefore, for each hour, we sample 270,000 satellite pixels (27 different satellite pixel sizes and 10,000 samples for each size), and for this example flight, we have a total of up to 1,080,000 possible satellite pixels in each of 4 hourly groups. Note that only ~10% of these samples are used in the analysis because we discarded a sampled satellite pixel if less than 75% of its area is covered by GeoTASO data. After applying this 75% area coverage filter, the actual sample size decreases when the pixel size increases. The number of samples is sufficient as our sensitivity tests indicate that the results do not change by halving the sample size. We also tested other choices of the coverage threshold over SMA in addition to 75% (not shown here). The results are similar for small pixels (< ~10 km<sup>2</sup>), as they are more likely to be covered by GeoTASO data regardless of the threshold value. For larger pixels (> ~15 km<sup>2</sup>), the satellite SGV is slightly lower when using 30% or 50% as the area coverage threshold because larger pixels act like smaller pixels when only partially covered. The threshold of 75% was chosen as a trade-off between sample size and representation.

Deleted:

Moved (insertion) [3]

Deleted: Note that the actual samples used in the analysis are less than 1,080,000 because we discarded a sampled satellite pixel if it is not covered by GeoTASO data for at least 75% of its area. Our sensitivity test indicates that the results do not change by halving the sample size

Deleted: .

Deleted: over SMA

Deleted: .

Deleted: .

## 2.5 Satellite pixel random sampling for temporal variability

We also quantify the temporal variability of the retrieved NO<sub>2</sub> VC within the same satellite pixels for different satellite pixel sizes. To calculate temporal variability within a hypothetical satellite pixel, we need GeoTASO data to cover the hypothetical satellite pixel at different times during the day. During the KORUS-AQ and 2017 SARP campaigns, rasters were treated as single units (Judd et al., 2019). Each raster produces a contiguous map of data that we consider as roughly representative of the mid-time of the raster. Unlike the calculation of SGV, which is based on data separated into hourly bins (section 2.4) to reduce the impact of temporal variability in the calculated spatial variability, the satellite pixel random sampling to assess temporal variability is based on rasters, and only conducted for days with multiple rasters. This is to ensure that the sampled hypothetical satellite pixels have multiple values at different times of the day, and hence maximize the sample size.

Deleted: .

To assess temporal variability within the hypothetical satellite pixels, we randomly select 50,000 pixel locations for each of the 27 hypothetical satellite pixel sizes, and use this same set of pixel locations to sample the GeoTASO data for each raster across all flights for a given day. This process is repeated for all days with multiple rasters, and the 75% of area coverage threshold is also applied. When there are two or more raster values of MEAN<sub>pixel</sub> for a given pixel location separated by time Dt, the temporal mean difference (TeMD) within the satellite pixel is calculated as:

$$\text{TeMD}(Dt) = \text{average}(|\text{MEAN}_{\text{pixel}}(t) - \text{MEAN}_{\text{pixel}}(t + Dt)|) \quad (1)$$



308 This procedure is repeated for each satellite pixel size.

## 309 2.6 Spatial structure function

310 Structure functions have been applied to in situ measurements and model-generated  
311 tropospheric trace gases to analyze their spatial and temporal variability in previous studies (Harris  
312 et al., 2001). The Spatial Structure Function (SSF) (Fishman et al., 2011; Follette-Cook et al., 2015)  
313 is an alternative measure to the satellite pixel random sampling described above for quantifying  
314 spatial variability, and in this work, we apply the SSF to GeoTASO data to assist our analysis of  
315 satellite SGV. The main difference between the two measures is that the SSF is based on individual  
316 GeoTASO data points, while the results from satellite pixel random sampling are based on sampled  
317 satellite pixels. The locations of the GeoTASO pixel centers are used to calculate the distances.  
318 The SSF as defined here follows Follette-Cook et al. (2015):

$$319 \quad f(NO_{2,VC}, D) = average(|NO_{2,VC}(x + D) - NO_{2,VC}(x)|) \quad (2)$$

320 where  $NO_{2,VC}$  is tropospheric  $NO_2$  VC.  $f(NO_{2,VC}, D)$  calculates the average of the absolute value  
321 of  $NO_{2,VC}$  differences across all data pairs (measured in the same hourly bin) that are separated by  
322 a distance  $D$ . To calculate SSF, the first step is the same as the first step of the satellite pixel  
323 random sampling: we group GeoTASO data hourly for each flight to reduce the impact of temporal  
324 variability of the GeoTASO data, and we only pair each GeoTASO data point with all the other  
325 GeoTASO data in the same hourly bin. More details on structure functions can be found in Follette-  
326 Cook et al. (2015).

## 327 2.7 WRF-Chem simulation

328 To briefly demonstrate the application of this technique on model evaluation and other  
329 species, we show results of a WRF-Chem simulation (Weather Research and Forecasting model  
330 coupled to Chemistry) with a resolution of  $3 \text{ km} \times 3 \text{ km}$  over SMA in [Section 4](#). The simulation  
331 used NCEP GDAS/FNL 0.25 Degree Global Tropospheric Analyses and Forecast Grids as initial  
332 and boundary conditions, and the model meteorological fields above the PBL were nudged 6-  
333 hourly. KORUS version 3 anthropogenic emissions and FINN version 1.5 fire emissions  
334 (Wiedinmyer et al., 2011) were used.

335

## 336 3. Results

337 In this section, we discuss the results for SGV over the different regions considered. Results  
338 are presented for the hypothetical satellite pixel random sampling for spatial variability and  
339 temporal variability, and for the spatial structure function analysis. We note that the three regions  
340 analyzed in this study are urban. Although we expect the results here to be generally applicable  
341 over urban regions, we have not tested the approach over cleaner background areas that are  
342 characterized by much less heterogeneity.

### 343 3.1 Sub-grid variability (SGV) within satellite pixels

Deleted: i

Deleted: Distance

Deleted: the Discussion section

Deleted: for spatial variability

348 SMA, the Busan region, and the LA Basin have different levels of pollution – the average  
 349 values of the GeoTASO NO<sub>2</sub> VC data over the SMA, the Busan region, and the LA Basin are  
 350  $2.3 \times 10^{16}$  molecules cm<sup>-2</sup>,  $1.1 \times 10^{16}$  molecules cm<sup>-2</sup>, and  $1.3 \times 10^{16}$  molecules cm<sup>-2</sup>, respectively.  
 351 Over the three regions, the mean values (MEAN<sub>pixel</sub>) and standard deviation (SD<sub>pixel</sub>) of the  
 352 hypothetical satellite pixels sampled over GeoTASO NO<sub>2</sub> VC data are different (Figure S3). This  
 353 is consistent with previous studies suggesting SGV can vary regionally (Judd et al., 2019;  
 354 Broccardo et al., 2018). However, we find that the normalized satellite SGV (calculated as the  
 355 ratio of SD<sub>pixel</sub> to MEAN<sub>pixel</sub> for a sampled pixel) is similar over each of the areas, regardless of  
 356 the absolute level of pollution as represented by MEAN<sub>pixel</sub> (Figure 4). Over SMA (Figure 4a), the  
 357 mean normalized satellite SGV of tropospheric NO<sub>2</sub> VC increases smoothly from ~10% for the  
 358 pixel size of 0.5 km × 0.5 km, to ~35% for the pixel size of 25 km × 25 km. The interquartile  
 359 variation of the satellite SGV also increases with satellite pixel sizes. The patterns of the sampled  
 360 satellite pixels over the Busan region (Figure 4b) and LA Basin (Figure 4c) are also found to be  
 361 similar to those over SMA. Furthermore, Figures S4 and S5 show that even the normalized SGV  
 362 of individual flights over the three domains generally follow the same pattern, except in the case  
 363 of the June 9 PM flight.

Deleted: absolute values of

Deleted: absolute values of

Deleted: that is discussed below

Deleted: .

364 We also compare normalized satellite SGV for different levels of pollution, regardless of  
 365 their regions (Figure S6). The normalized satellite SGV for the less polluted pixels (MEAN<sub>pixel</sub>  
 366 being lower than the average value of all pixels, i.e.,  $2 \times 10^{16}$  molecules cm<sup>-2</sup>) also shows an overall  
 367 similar pattern as for the more polluted pixels (MEAN<sub>pixel</sub> being higher than the average value of  
 368 all pixels). We notice that at small pixel sizes, less polluted pixels have higher normalized satellite  
 369 SGV, possibly contributed by relatively higher retrieval noise at lower pollution levels.

Deleted: .

... [1]

370 We show the normalized SGV for individual rasters over SMA (Figure 5) to indicate the  
 371 uncertainty range of the normalized SGV shown in Figure 4. The spread of SGV across different  
 372 individual rasters represents the uncertainties of using the averaged normalized SGV for a specific  
 373 case. Note that the variation of normalized SGV with pixel size for individual rasters generally  
 374 follows the same pattern (i.e., increases with satellite pixel size), especially when the pixel size is  
 375 small ( $\leq 10$  km × 10 km). The normalized SGV increases from ~10% to ~25%, with the uncertainty  
 376 range consistently being  $\pm 5\%$  when the pixel size is smaller than 10 km × 10 km. When the pixel  
 377 size is larger than 10 km × 10 km, the uncertainty range broadens with pixel sizes from  $\pm 5\%$  (10  
 378 km × 10 km) to  $\pm 15\%$  (25 km × 25 km). This means that when the satellite pixel size is large,  
 379 using the mean normalized SGV in Figure 4 to represent specific cases may lead to larger  
 380 uncertainties. Below the resolution of 10 km × 10 km, SGV can be characterized by the mean  
 381 value with relatively smaller uncertainty ( $\pm 5\%$ ) and hence high confidence, even with large diurnal  
 382 or day-to-day variations. The spatial resolutions of TEMPO, GEMS, Sentinel-4, and TROPOMI  
 383 (TROPOspheric Monitoring Instrument, Veefkind et al., 2012; Griffin et al., 2019; van Geffen et  
 384 al., 2019) are within this  $\leq 10$  km × 10 km range, while the resolution of OMI (Levelt et al., 2006;  
 385 2018) is not. This means that applying this study (e.g., Figure 4) to OMI for a specific case study  
 386 (e.g., a specific day) requires extra caution.

Deleted: Therefore, our analysis reveals a threshold for spatial resolution at about 10 km × 10 km.

Deleted: this

Deleted: Ozone Monitoring Instrument,

387 The GeoTASO data located closely in space may be sampled at slightly different times for  
 388 the same flight. To explore the impact of temporal variability on this SGV analysis, we performed  
 389 two sensitivity tests. The typical time period for a complete flight is ~4 hours. In the first test, we  
 390 sampled GeoTASO data with hypothetical satellite pixels grouped by each complete flight, rather



than grouping the data by each hour (i.e., hourly bins). The resulting patterns and relationships are similar to those derived from grouping data into hourly bins, except that the normalized satellite SGV increases ~5% for small pixels due to temporal variability (Figure S7a). In the second test, we sampled GeoTASO data with hypothetical satellite pixels grouped by each raster. The results are still similar to those derived from grouping data into hourly bins (Figure 4), except that the normalized satellite SGV increases ~1% for small pixels due to the inclusion of temporal variability (Figure S7b). This is because sampling by raster includes smaller temporal variability than sampling by flight, but larger temporal variability than sampling by hourly bins.

The three regions investigated in this work have different levels of urbanization and air pollution (Figures 1 and S2). PBL conditions are also different in the morning and afternoon (Figure S8). The similarity of the relationships between the satellite pixel size and the normalized satellite SGV over these different regions (Figure 4) suggests that this relationship may be generalizable to NO<sub>2</sub> VC over urban regions with different levels of urbanization and air pollution, and different PBL conditions. Moreover, Figures 4 and 5 point to the possibility of developing a generalized look-up table for the expected normalized satellite SGV for NO<sub>2</sub> VC over urban regions at different satellite pixel sizes, especially for small pixel sizes (e.g., TEMPO, GEMS, and TROPOMI). This would be useful in satellite design, satellite retrieval evaluation and interpretation, and satellite-in situ data comparisons. For example, the satellite pixel size of tropospheric NO<sub>2</sub> VC retrievals from GEMS, TEMPO, TROPOMI, and OMI are highlighted in Figure 4. Following Judd et al. (2019), we choose 3 km × 3 km, 5 km × 5 km, 7 km × 8 km, and 18 km × 18 km pixels to represent the expected area of the satellite pixels for TEMPO (2.1 km × 4.4 km), TROPOMI (3.5 km × 7 km), GEMS (7 km × 8 km), and OMI (18 km × 18 km), respectively. The expected normalized satellite SGV for TEMPO, TROPOMI, GEMS, and OMI are 15–20%, ~20%, 20–25%, and ~30%, respectively. Taking the TEMPO example, this implies that the satellite SGV could potentially lead to uncertainties of 15–20% in a validation exercise comparing a satellite retrieval with local measurements of NO<sub>2</sub> VC, from a Pandora spectrometer for example, that may be unrepresentative of the wider pixel area.

### 3.2 Temporal variability (TeMD) within the same satellite pixels

In addition to satellite spatial SGV, we also analyze the temporal variability (i.e., TeMD) within the same hypothetical satellite pixels. Figure 6 shows TeMD of satellite retrieved tropospheric NO<sub>2</sub> VC over SMA as a function of hypothetical satellite pixel size and the separation time (Dt) between flight rasters as described in Section 2.5. The results for 27 satellite pixel sizes analyzed are shown by different colors, while results for selected satellite pixel sizes are highlighted by thicker lines. For all the pixel sizes, TeMD increases monotonically with the time difference Dt between two sampled raster values within the same pixel. The TeMD of tropospheric NO<sub>2</sub> VC is around  $0.75 \times 10^{16}$  molecules cm<sup>-2</sup> for a Dt of 2 hours over SMA for all the sampled satellite pixel sizes, and increases to  $\sim 2 \times 10^{16}$  molecules cm<sup>-2</sup> for Dt of 8 hours. This indicates that, along with improvements in the satellite retrieval spatial resolution with smaller pixels, improving the satellite retrieval temporal resolution with higher frequency measurements is also an effective way to enhance capability in resolving variabilities of NO<sub>2</sub>.

To investigate the TeMD shown in Figure 6 we consider the particular factors driving NO<sub>2</sub> variability over SMA. NO<sub>2</sub> has a relatively short lifetime (~ a few hours) and a strong diurnal cycle due to emission activities, chemistry and changing photolysis rate (Fishman et al., 2011; Follette-

**Deleted:** We tested the sensitivity of the results over SMA to sampling GeoTASO data with hypothetical satellite pixels grouped by complete flight, rather than grouping the data by time in hourly bins. The resulting patterns and relationships are similar, except that the normalized satellite SGV increases ~5% for pixels of small sizes due to the inclusion of temporal variability (Figure S8a). We also tested the results for sampling satellite pixels by raster instead of within hourly bins. The results are again similar to Figure 4, except that the normalized satellite SGV increases ~1% for pixels of small sizes due to the inclusion of temporal variability (Figure S8b).

**Deleted:** 9

**Deleted:** sub-satellite local ground

**Deleted:** as might be obtained from a Pandora spectrometer. As a result, we should caution that calculating a pixel mean bias when evaluating against local measurements within the pixel sometimes may be optimistic due to the cancellation of sub-grid positive and negative biases.

**Deleted:** s

**Deleted:** ,

465 Cook et al., 2015). The diurnal cycle of the PBL may also play a large role because horizontal  
 466 dispersion occurs as the PBL thickens during the day. Early in the morning, the PBL is low (~1400  
 467 m during 9:00-11:00 in SMA during KORUS-AQ) and strong source locations are evident such as  
 468 traffic on major highways, etc. As the day progresses, the PBL height increases (~1800 m during  
 469 15:00-17:00; Figure S8) due to enhanced convection, which further induces a stronger horizontal  
 470 divergence at the top of the convective cell that allows for greater horizontal dispersion to take  
 471 place along with the divergence. By early afternoon, emissions from all the major sources in the  
 472 central region have mixed together to form a wide area of high pollution over the urban center with  
 473 strong gradients of decreasing NO<sub>2</sub> out to the surrounding areas. In addition, changing wind  
 474 conditions (speed and direction; Figure S9) during the day can also lead to a shift in pollution  
 475 pattern, and result in different pollution conditions for the same pixel at different time of a day.  
 476 For example, Raster 1 of the 0609AM (9.17 local time) and Raster 2 of 0609PM (17 local time)  
 477 are used to calculate TeMD for Dt equals 8 hours. The differences in wind conditions (Figure S9)  
 478 and the pollution patterns (Figure 2) are large. Judd et al. (2018) point out that the topography over  
 479 SMA also plays a role in the ability to mix horizontally as the PBL grows. Therefore, the TeMD  
 480 can be large between morning and afternoon (i.e., for Dt larger than 6 hours).

Deleted: s

Deleted: s

Deleted: As the day progresses, the PBL height increases (~1800 m during 15:00-17:00; Figure S9) allowing for greater horizontal mixing to take place.

481 For a small Dt (2 or 4 hours), TeMD increases at higher spatial resolution (i.e., smaller  
 482 pixel size). This is especially true for short time periods (e.g., 2 hours and 4 hours), which is more  
 483 important for the GEO satellite measurements. For example, for Dt of 2 hours, TeMD for satellite  
 484 pixels of 1 km × 1 km is about 0.80×10<sup>16</sup> molecules cm<sup>-2</sup>, while TeMD for satellite pixels of 25  
 485 km × 25 km is about 0.73×10<sup>16</sup> molecules/cm<sup>2</sup> (~9% lower); when Dt is 4 hours, TeMD for satellite  
 486 pixels of 1 km × 1 km is about 1.3×10<sup>16</sup> molecules cm<sup>-2</sup>, while TeMD for satellite pixels of 25 km  
 487 × 25 km is about 1.1×10<sup>16</sup> molecules/cm<sup>2</sup> (~15% lower). This indicates that when decreasing pixel  
 488 size, the temporal variability of the retrieved values will increase, even though the normalized  
 489 satellite spatial SGV decreases. This is expected because averaging over a larger region with high  
 490 small-scale spatial variability smooths out temporal variability, and therefore produces smaller  
 491 hourly differences. Our finding here is consistent with that of Fishman et al. (2011).

Deleted: when increasing theat higher

Deleted: satellite retrieval

Deleted: increasing

Deleted: the satellite retrieval spatial resolution (decreasing

Deleted: )

Deleted: so

Deleted: ing

492 As the time difference Dt increases, the temporal variability TeMD increases for all pixel  
 493 sizes. However, the TeMD is now greater at large pixel size which is in contrast to the higher  
 494 TeMD at small pixel size for shorter Dt. This is a result of the pollution pattern that develops over  
 495 the SMA during the day (June 9<sup>th</sup>, 2019) as described above. The higher TeMD reflects the fact  
 496 that many of the large pixels now span the strong NO<sub>2</sub> gradient between the urban and surrounding  
 497 area resulting in a much higher spatial variability than earlier in the day at a spatial scale not  
 498 captured with the smaller pixels. As a caution, we note that TeMD for 8 hours is determined by  
 499 only the difference between Raster 1 of the 0609AM and Raster 2 of 0609PM (Figure 2), and that  
 500 the regional coverage for Raster 2 of 0609PM is different from the coverage of the other PM rasters.  
 501 Therefore, the relationship of TeMD and spatial resolution for a large Dt (e.g., 6 or 8 hours) over  
 502 SMA requires further study.

Formatted: Superscript

503 GeoTASO data over the Busan region is limited. Given the fewer flights, we are not able  
 504 to show how TeMD changes with Dt over the Busan region in this study. However, we are able to  
 505 show the relationship between TeMD and satellite pixel sizes. During KORUS-AQ, there were  
 506 only two rasters sampled over Busan with a Dt of 2 hours (Figure S10). For this Dt of 2 hours,  
 507 TeMD increases slightly at higher satellite retrieval spatial resolution (smaller pixel size). More  
 508 data over the Busan region would help significantly for this analysis. For the LA Basin GeoTASO

Deleted: 0

Deleted: when increasing the

data, sampled hypothetical satellite pixels show TeMD increases at higher spatial resolution for the available Dt equal to 4 and 8 hours (Figure S11). However, TeMD is fairly constant at these two time differences which is different to what was observed over SMA (Figure 6). We note that with only 2 flight days of flight data, the GeoTASO data over LA is also limited, which may be the main driver of the difference. Besides the limited data, one possible reason is the different wind fields over the two regions. As mentioned previously, Raster 1 of the 0609AM and Raster 2 of 0609PM are used to calculate TeMD for Dt equals 8 hours over SMA. The differences in wind direction (Figure S9) for the two rasters are large (almost opposite in some cases). However, over LA, the differences in wind direction (Figure S12) for the two rasters (Rasters 1 and 3 for 0627 flight) are relatively small, compared to the differences over SMA. Despite the limited sample sizes, TeMD increases when increasing the satellite retrieval spatial resolution over both the Busan region and the LA Basin, which is consistent with the relationships over the SMA for a small Dt.

Deleted: over the LA Basin, for a given Dt, TeMD increases when increasing the satellite retrieval spatial resolution (smaller pixel size) for Dt equal to 4 and 8 hours (Figure S11).

Deleted:

### 3.3 Results from Spatial Structure Function (SSF)

In this section, we show the analysis of SSF over SMA (Figure 7) as a complement to our analysis in Section 3.1. As mentioned before, SSF and SGV are different measures of spatial variability and are not directly comparable. This is because SSF is calculated based on differences between a single GeoTASO measurement and all the other GeoTASO measurements on the map, while SGV is derived based on variation among all the GeoTASO measurements within a hypothetical satellite pixel unit. SSF measures the averaged spatial difference at a given distance, while SGV directly quantifies the expected spatial variability within a satellite pixel at a given size. As both SSF and SGV are related to spatial variability, we include SSF in this study as an extension to SGV.

Figure 7a shows that the SSF in SMA initially increases with the distance between data points, peaks at around 40-60 km during most flights, and then decreases with distance between 60 and 140 km. The number of paired GeoTASO data points when the distance is larger than 100 km is relatively small (Figure S13) therefore conclusions beyond this distance are not included in this analysis. The increases in SSF for distances in the range of 1-25 km (Figure 7b) are consistent with the relationship between pixel sizes and the normalized satellite SGV shown in Figure 4. For example, over the 1-25 km range, Fig 4a shows the median increases from around 8% to around 28%, an increase by a factor of 3.5, and the black line in Figure 7 shows an approximately similar factor (from  $0.33 \times 10^{16}$  molecules/cm<sup>2</sup> for 1 km to  $1.5 \times 10^{16}$  molecules/cm<sup>2</sup> for 25 km). This increase of SSF between 1-25 km is also seen over the Busan region and the LA Basin (Figure S14). We also notice that SSF shows a relatively strong dependence on the particular GeoTASO flight, while SGV is less sensitive, especially for small pixel sizes.

Deleted: 2

Deleted: 3

The shapes of the SSF are generally consistent with previous studies for modeled or in situ observations of NO<sub>2</sub> (Fishman et al., 2011; Follette-Cook et al., 2015). Previous studies also suggest that different aircraft campaigns may share the common shape of SSF but different magnitudes, which is strongly related to the fraction of polluted samples versus samples of background air in the campaign (Crawford et al., 2009; Fishman et al., 2011). Differences in the shape and size of particular cities also contribute to the differences in the SSF. For example, at a certain distance SSF may compare polluted areas within the same urban region, while over a different smaller city, the comparison at the same distance reveals the gradient between the polluted city and cleaner surrounding background air, so resulting in different peak values. Valin

et al. (2011) found that the maximum in OH feedback in a NO<sub>x</sub>-OH steady-state relationship corresponds to a NO<sub>2</sub> e-folding decay length of 54 km in 5m/s winds. This may partially explain the peak between 40–60 km in SSF. As shown in Figures 2 and S7, the overall spatial variability over SMA is higher in the afternoon. Over SMA, the SSF in the morning is generally smaller than in the afternoon, indicating higher spatial variability of tropospheric NO<sub>2</sub> VC in the afternoon (see also Judd et al., 2018). As described in Section 2.6, SSF is calculated based on hourly binned data. However, the overall shapes of SSF (Figure S15) calculated on raster basis are similar to SSF calculated on hourly basis (Figure 7).

Previous studies (Fishman et al., 2011; Follette-Cook et al., 2015) used SSF values at a particular distance to indicate the satellite precision requirement at a corresponding resolution in order to resolve spatial structure over the pixel scale. For GEMS, the expected spatial differences over the scale of its pixel for the SMA and Busan regions are  $\sim 7.5 \times 10^{15}$  molecules cm<sup>-2</sup> and  $\sim 3.5 \times 10^{15}$  molecules cm<sup>-2</sup>, respectively, taking the SSF values at 5 km to be representative. For TEMPO, the spatial difference is  $\sim 2.8 \times 10^{15}$  molecules cm<sup>-2</sup> over LA Basin taking the SSF value at 3 km. Assuming the NO<sub>2</sub> measurement precision requirement to be  $1 \times 10^{15}$  molecules cm<sup>-2</sup> for both TEMPO and GEMS (Chance et al., 2013; Kim et al., 2020), the expected spatial differences over the three regions are considerably higher than the precision requirement and should be easily characterized by both the GEMS and TEMPO missions.

#### 4. Discussions and implications

The relationship between satellite pixel sizes and the normalized satellite SGV is fairly robust over the three different urban regions studied here, and Figure 4 points to the possibility of developing a generalized look-up table if more data were available in other urban regions. We note that the GeoTASO data used in this study were sampled during spring and summer. In our future study, we will include more GeoTASO data in the analysis to test the applicability of the look-up table approach under different seasonal conditions and sources. A generalized relationship between satellite pixel sizes and the temporal variability (Figure 6) is not as evident as the relationship between satellite pixel sizes and the normalized satellite SGV due to limited data. However, it is still useful for satellite observations over SMA, which is in the GEMS domain and should be helpful in satellite retrieval interpretation.

Previous studies recognized the challenges in satellite validation/evaluation for NO<sub>2</sub> retrievals due to satellite SGV and representativeness error of in situ measurements (e.g., Nowlan et al., 2016, 2018; Judd et al., 2019; Pinardi et al., 2020; Tack et al., 2020). The gapless airborne mapping datasets of GeoTASO with sufficient spatiotemporal resolution are a promising way to address the issue of satellite SGV and representativeness errors in satellite validation/evaluation (e.g., Nowlan et al., 2016, 2018; Judd et al., 2019).

Challenges due to SGV also have implications for other trace gas column measurements. For example, in Tang et al. (2020), satellite SGV and representativeness errors of in situ measurements introduced uncertainties in validation of CO retrievals from the MOPITT (Measurement Of Pollution In The Troposphere) satellite instrument. Normalized SGV of the GeoTASO tropospheric NO<sub>2</sub> VC might serve as an upper bound to the SGV of CO, SO<sub>2</sub> and other species that share common source(s) with NO<sub>2</sub> but with relatively longer lifetimes than NO<sub>2</sub>, even if their spatial distributions have different patterns (e.g., Chong et al., 2020). For example, at the

**Deleted:** discussed here (Figure 7)

**Deleted:** bin

**Deleted:** We also include SSF that is calculated within rasters in the supplement (Figure S14). T

**Deleted:** 4

**Moved down [2]:** This study also has implications for satellite validation and evaluation, and satellite-in situ data comparisons of other trace gas species.

**Deleted:** This study also has implications for satellite satellite validation and evaluation, and satellite-in situ data comparisons of other trace gas species. Our initial motivation to study satellite SGV arose from our previous work on validation of MOPITT (Measurements of Pollution in the Troposphere) CO retrievals over urban regions (Tang et al., 2020). In that study, we compared the satellite retrievals with aircraft profiles, and realized that satellite SGV and representativeness error of aircraft profiles in the comparisons to MOPITT retrievals introduced uncertainties in the validation results. Previous studies have noticed the same issue for NO<sub>2</sub> (e.g., Nowlan et al., 2016, 2018; Judd et al., 2019; Pinardi et al., 2020; Tack et al., 2020), but this issue is difficult to address and quantify due to the limited spatial coverage of most aircraft observations. Even though only a few trace gas species are routinely retrieved, the gapless raster datasets of GeoTASO are a possible way to address this problem.

**Moved (insertion) [2]**

**Deleted:** This study also has implications for satellite validation and evaluation, and satellite-in situ data comparisons of other trace gas species. The

**Deleted:** n

**Deleted:** have

**Formatted:** Subscript

**Deleted:** may

647 resolution of 22 km × 22 km (resolution of MOPITT CO retrievals), the expected normalized  
648 satellite SGV of tropospheric NO<sub>2</sub> VC is ~30%. Therefore, we might expect the normalized  
649 satellite SGV for tropospheric CO VC to be lower than this value.

650 To demonstrate this idea, we use the WRF-Chem regional model as an intermediary step.  
651 At the model resolution, if the SVG of the WRF-Chem model and GeoTASO NO<sub>2</sub> VC agree  
652 reasonably well, then the model can be used to predict the SVG of other species that are chemically  
653 constrained with NO<sub>2</sub> at the model and coarser resolutions. This is shown in Figure 8 which  
654 illustrates how SGV varies with satellite pixel size for NO<sub>2</sub> VC, CO VC, SO<sub>2</sub> VC, and HCHO VC  
655 calculated from a WRF-Chem simulation. The modeled NO<sub>2</sub>, CO, SO<sub>2</sub>, and HCHO concentrations  
656 are converted to VC, and are filtered to match the rasters of GeoTASO measurements (Figure S16).  
657 As expected, SGV of modeled NO<sub>2</sub> VC is higher than SGV of modeled CO VC, SO<sub>2</sub> VC, and  
658 HCHO VC. We also notice that SGV for modeled NO<sub>2</sub> VC, CO VC, SO<sub>2</sub> VC, and HCHO VC  
659 increases with pixel size, which is similar to that for GeoTASO measurements. The SGV for  
660 GeoTASO NO<sub>2</sub> shown in this figure (black lines) is calculated based on GeoTASO data that are  
661 regridded to the WRF-Chem grid (3 km × 3 km), making it slightly different from that in Figure  
662 4. We note that the modelled NO<sub>2</sub> SGV is greater than that calculated from the GeoTASO data  
663 indicating that further work is required to reconcile difference due to model descriptions of  
664 emissions, chemistry and transport. And ideally, dense GeoTASO-type measurements of CO and  
665 other species would allow for a more comprehensive assessment of this approach.

666 This study is also relevant to model comparison and evaluation with *in situ* observations.  
667 Whenever *in situ* observations are compared to grid data (e.g., comparisons between satellite  
668 retrievals and *in situ* observations, comparisons between grid-based model and *in situ* observations,  
669 and *in situ* data assimilation), SGV will introduce uncertainties that need to be quantified to better  
670 interpret and understand the comparison results. For example, we note that at the resolution of 14  
671 km×14 km (a typical resolution for the forward-looking Multi-Scale Infrastructure for Chemistry  
672 and Aerosols Version 0; MUSICA-V0, <https://www2.acom.ucar.edu/sections/multi-scale-chemistry-modeling-musica>; Pfister et al. (2020)), Figure 8 shows that the expected normalized  
673 SGV of tropospheric NO<sub>2</sub> VC is ~25-30%. This suggests that when comparing model simulations  
674 at coarser resolution with local observations of tropospheric NO<sub>2</sub> VC, a larger normalized SGV  
675 than this ~25-30% might be expected. If comparing for a specific vertical layer instead of vertical  
676 column, an even larger normalized SGV may occur.

678 For data assimilation and inverse modeling application (e.g., top-down emission  
679 estimations from satellite observations), it is essential to accurately characterize the observation  
680 error covariance matrix **R** (Janjic et al., 2017). The first component of **R** is the instrument error  
681 covariance matrix due to instrument noise and retrieval uncertainty in the case of trace gas satellite  
682 data. The second component is the representation error covariance matrix, arising from  
683 fundamental differences of the atmospheric sampling, typically when assimilating a local point  
684 measurement into a grid-based model (Boersma et al., 2016). The observation error covariance due  
685 to representativeness error is difficult to define, but can be parameterized when calculating super  
686 observations by inflating the observation error variances (Boersma et al., 2016) and quantified by  
687 a posteriori diagnostics estimation (Gaubert et al. 2014). Knowledge of the fine-scale model sub-  
688 grid variability is therefore essential to verify those assumptions and inform error statistics for  
689 application to chemical data assimilation studies. Our results suggest large potential improvements  
690 in emission estimates when assimilating high spatial resolution TROPOMI and GEO satellite data

Deleted: .  
Deleted: t

Deleted: resolution  
Deleted: at  
Deleted: formaldehyde (  
Deleted: )  
Deleted: S15

Deleted: Note that a more comprehensive comparison requires further work and ideally actual

Deleted: to address differences due to local sources on the background concentrations  
Deleted: local  
Deleted: local  
Deleted: local  
Deleted: local

Deleted:  
Deleted: [2020]  
Deleted: satellite  
Deleted: W  
Deleted: a  
Deleted: local  
Deleted: for  
Deleted: larger  
Deleted: may



with SGV of ~10%–20% (Figure 4), compared to OMI data with SVG of ~30% (Figure 4), in line with the existing literature for NO<sub>2</sub> (e.g., Valin et al., 2011). We have also shown that significant temporal variability of NO<sub>2</sub> is expected at higher spatial resolutions. This observed signal will open new avenue for space-based monitoring of atmospheric chemistry and will reduce errors of inverse estimates of fluxes.

## 5. Conclusions

Satellite SGV is a key issue in interpreting satellite retrieval results. Quantifying studies have been lacking due to limited observations at high spatial and temporal resolution. In this study, we have quantified likely GEO satellite SGV by using GeoTASO measurements of tropospheric NO<sub>2</sub> VC over the urbanized and polluted Seoul Metropolitan Area (SMA) and the less-polluted Busan region during KORUS-AQ, and the Los Angeles (LA) Basin during the 2017 SARP campaigns. The main findings of this work are the following:

- (1) The normalized satellite SGV increases with pixel size, based on random sampling of hourly GeoTASO data, from ~10% (±5% for specific cases such as an individual day/time of day) for a pixel size of 0.5 km × 0.5 km to ~35% (±10% for specific cases such as an individual day/time of day) for the pixel size of 25 km × 25 km. This conclusion holds for all of the three urban regions in this study, despite their different levels of urbanization and pollution, and for time of day being morning or afternoon.
- (2) Due to its relatively shorter atmospheric lifetime, normalized satellite SGV of tropospheric NO<sub>2</sub> VC could serve as an upper bound to satellite SGV of CO, SO<sub>2</sub> and other species that share common source(s) with NO<sub>2</sub>. This conclusion is supported by high-resolution WRF-Chem simulations.
- (3) The temporal variability (TeMD) increases with sampling time differences (Dt) over SMA. TeMD ranges from ~0.75×10<sup>16</sup> molecules cm<sup>-2</sup> at Dt of 2 hours to ~2×10<sup>16</sup> molecules cm<sup>-2</sup> (about three times higher) at Dt of 8 hours. TeMD is caused by temporal variation in emission activities, photolysis, and meteorology throughout the day. Improving the satellite retrieval temporal resolution is an effective way to enhance the capability of satellite products in resolving temporal variability of NO<sub>2</sub>.
- (4) Temporal variability (TeMD) increases as pixel size decreases in SMA when time difference is less than 4 hours. Analysis confidence at greater time differences would require more flight datasets with longer time separations during the day. For example, when Dt is 2 hours, TeMD for satellite pixels with the size of 25 km × 25 km is about 20% lower compared to TeMD for satellite pixels with the size of 1 km × 1 km. Thus, ideally, temporal resolution should be increased along with any increase in spatial resolution in order to enhance the accuracy of satellite products.
- (5) The spatial structure function (SSF) at first increases with the distance between points, peaking at around 40–60 km during most flight days, before decreasing at greater distances. This is generally consistent with previous studies.
- (6) SSF analyses suggest that GEMS will encounter NO<sub>2</sub> VC pixel scale spatial differences of ~7.5×10<sup>15</sup> and ~3.5×10<sup>15</sup> molecules cm<sup>-2</sup> over the SMA and Busan regions, respectively. TEMPO will encounter NO<sub>2</sub> VC spatial differences at its pixel scale of ~2.8×10<sup>15</sup> molecules

Deleted: high-resolution

Deleted: hypothetical satellite

Deleted: s

Deleted: satellite pixel

Deleted: study

Deleted: ,

Deleted: ,

Deleted: The

Deleted: but have relatively longer lifetime,

Deleted: as

Deleted: the

Deleted: within the same hypothetical satellite pixels

Deleted: likely impacted by the short lifetime and diurnal cycle of NO<sub>2</sub> due to

Deleted: and

Deleted: rate

Deleted: ,

Deleted: the

Deleted: and PBL evolution during

Deleted: ies

Deleted: when increasing the satellite retrieval spatial resolution (i.e., smaller pixel size)

Deleted: -

Formatted: Key Points, Space Before: 0 pt

Deleted: ly

Deleted: between data points,

Deleted: peaks at

Deleted: , and then decreases with distance



cm<sup>-2</sup> over the LA Basin. These differences should be easily resolved by the instruments at the stated measurement precision requirement of  $1 \times 10^{15}$  molecules cm<sup>-2</sup>.

- (7) These findings are relevant to future satellite design and satellite retrieval interpretation, especially now with the deployment of the high-resolution GEO air quality satellite constellation, GEMS, TEMPO, and Sentinel-4. This study also has implication for satellite product validation and evaluation, satellite-in situ data comparisons, and more general point-grid data comparisons. These share similar issues of sub-grid variability and the need for quantification of representativeness error.

We note that this study has some uncertainties and limitations. (1) The variability at a resolution finer than  $250 \text{ m} \times 250 \text{ m}$  (i.e., GeoTASO's resolution) may introduce uncertainties to the analysis here, although this is beyond the scope of this study. (2) Even though a large number of GeoTASO retrievals have been analyzed in this study, we would still benefit from more GeoTASO flights with a broader spatiotemporal coverage. More GeoTASO-type data over the Busan region and LA Basin will help in testing the consistence in TeMD over different regions. (3) The KORUS-AQ campaign was conducted in Spring (May and June), and the 2017 SARP campaign was also conducted in June. More GeoTASO-type measurements over South Korea during different season(s) would be particularly helpful to understand and generalize the findings in this study. (4) The three regions analyzed in this study are urban regions, and the results are not tested over cleaner background areas that may be characterized by less heterogeneity.

This work demonstrates the value of continued flights of GeoTASO-type instruments for obtaining continuous, high spatial resolution data several times a day for assessing SGV. This will be a particularly useful reference in the comparisons of satellite retrievals and in situ measurements that may have representativeness errors.

Deleted: high-resolution measurements

Deleted: , particularly over the Busan region

## Acknowledgement

The authors thank the GeoTASO team for providing the GeoTASO measurements. The authors thank the KORUS-AQ and SARP team for the campaign data. We thank the DIAL-HSRL team for the mixing layer height data (available at <https://www-air.larc.nasa.gov/cgi-bin/ArcView/korusaq>). Tang was supported by a NCAR Advanced Study Program Postdoctoral Fellowship. Edwards was partially supported by the TEMPO Science Team under Smithsonian Astrophysical Observatory Subcontract SV3-83021. The National Center for Atmospheric Research (NCAR) is sponsored by the National Science Foundation. The authors thank Ivan Ortega and Sara-Eva Martinez-Alonso for helpful comments on the paper.

## Data availability

The KORUS-AQ and SARP data are available at <https://www-air.larc.nasa.gov/cgi-bin/ArcView/korusaq> and <https://www-air.larc.nasa.gov/cgi-bin/ArcView/lmos>, respectively.

## Reference

Al-Saadi, Jassim, Gregory Carmichael, James Crawford, Louisa Emmons, Saewung Kim, Chang-Keun Song, et al. KORUS-AQ: An international cooperative air quality field study in Korea, the

Deleted:

Deleted: (2014)

828 KORUS-AQ white paper, 2014 ([https://espo.nasa.gov/korus-aq/content/](https://espo.nasa.gov/korus-aq/content/KORUS-AQ_White_Paper) KORUS-  
829 AQ\_White\_Paper), 2014.

830 Boersma, K. F., Vinken, G. C. M., and Eskes, H. J.: Representativeness errors in comparing  
831 chemistry transport and chemistry climate models with satellite UV–Vis tropospheric column  
832 retrievals, *Geosci. Model Dev.*, 9, 875–898, <https://doi.org/10.5194/gmd-9-875-2016>, 2016.

833 Broccardo, S., Heue, K.-P., Walter, D., Meyer, C., Kokhanovsky, A., van der A, R., Piketh, S.,  
834 Langerman, K., and Platt, U.: Intra-pixel variability in satellite tropospheric NO<sub>2</sub> column densities  
835 derived from simultaneous space-borne and airborne observations over the South African  
836 Highveld, *Atmos. Meas. Tech.*, 11, 2797–2819, <https://doi.org/10.5194/amt-11-2797-2018>, 2018.

837 [Chance, K., Liu, X., Suleiman, R. M., Flittner, D. E., Al-Saadi, J. and Janz, S. J.: Tropospheric](#)  
838 [emissions: Monitoring of pollution \(TEMPO\), Proceedings of SPIE, Vol. 8866, Earth Observin](#)  
839 [Systems XVIII, 88660D \(September 23, 2013\), San Diego, CA USA, 2013.](#)

840 Ching, J., Herwehe, J., and Swall, J.: On joint deterministic grid modeling and sub-grid variability  
841 conceptual framework for model evaluation, *Atmos. Environ.*, 40, 4935–4945, 2006.

842 Choi, S., Lamsal, L. N., Follette-Cook, M., Joiner, J., Krotkov, N. A., Swartz, W. H., Pickering,  
843 K. E., Loughner, C. P., Appel, W., Pfister, G., Saide, P. E., Cohen, R. C., Weinheimer, A. J., and  
844 Herman, J. R.: Assessment of NO<sub>2</sub> observations during DISCOVER-AQ and KORUS-AQ field  
845 campaigns, *Atmos. Meas. Tech.*, 13, 2523–2546, <https://doi.org/10.5194/amt-13-2523-2020>, 2020.

846 [Chong, H.; Lee, S.; Kim, J.; Jeong, U.; Li, C.; Krotkov, N.; Nowlan, C.; Al-Saadi, J.; Janz, S.;](#)  
847 [Kowalewski, M.; et al. High-resolution mapping of SO<sub>2</sub> using airborne observations from the](#)  
848 [GeoTASO instrument during the KORUS-AQ field study: PCA-based vertical column retrievals.](#)  
849 [Remote Sens. Environ., 241, 111725, 2020.](#)

850 [Courrèges-Lacoste, G. B., Sallusti, M., Bulsa, G., Bagnasco, G., Veihelmann, B., Riedl, S., Smith,](#)  
851 [D. J., and Maurer, R.: The Copernicus Sentinel 4 mission: a geostationary imaging UVN](#)  
852 [spectrometer for air quality monitoring, Proceedings Volume 10423, Sensors, Systems, and Next-](#)  
853 [Generation Satellites XXI, 1042307, <https://doi.org/10.1117/12.2282158>, 2017.](#)

854 Crawford, J.H.: Assessing scales of variability for constituents relevant to future geostationary  
855 satellite observations and models of air quality. *AGU, 90(52), Fall Meet. Suppl., Abstract*  
856 *A53Ae0237*, 2009.

857 [Crawford, J. H., et al., The Korea-United States Air Quality \(KORUS-AQ\) Field Study, Elementa,](#)  
858 [in press, 2021.](#)

859 [Denby, B., Cassiani, M., de Smet, P., de Leeuw, F., and Horálek, J.: Sub-grid variability and its](#)  
860 [impact on European wide air quality exposure assessment, Atmos. Environ., 45, 4220–4229, 2011.](#)

861 [Deeter, M. N., Edwards, D. P., Francis, G. L., Gille, J. C., Mao, D., Martínez-Alonso, S., Worden,](#)  
862 [H. M., Ziskin, D., and Andreae, M. O.: Radiance-based retrieval bias mitigation for the MOPITT](#)  
863 [instrument: the version 8 product, Atmos. Meas. Tech., 12, 4561–4580,](#)  
864 [https://doi.org/10.5194/amt-12-4561-2019, 2019.](#)

**Deleted:** Chance, K., Liu, X., Suleiman, R. M., Flittner, D. E., Al-Saadi, J., & Janz, S. J. (2013, September). Tropospheric emissions: monitoring of pollution (TEMPO). In *Earth Observing Systems XVIII* (Vol. 8866, p. 88660D). International Society for Optics and Photonics. .

**Deleted:** Chong, H., Lee, S., Kim, J., Jeong, U., Li, C., Krotkov, N. A., ... & Ahn, M. H. (2020). High-resolution mapping of SO<sub>2</sub> using airborne observations from the GeoTASO instrument during the KORUS-AQ field study: PCA-based vertical column retrievals. *Remote Sensing of Environment*, 241, 111725.

**Deleted:** Courrèges-Lacoste, G. B., Sallusti, M., Bulsa, G., Bagnasco, G., Veihelmann, B., Riedl, S., ... & Maurer, R. (2017, September). The copernicus sentinel 4 mission: a geostationary imaging UVN spectrometer for air quality monitoring. In *Sensors, Systems, and Next-Generation Satellites XXI* (Vol. 10423, p. 1042307). International Society for Optics and Photonics. .

**Deleted:** , et al., 2009

**Deleted:** .

**Deleted:** .

**Deleted:** Denby, B., Cassiani, M., de Smet, P., de Leeuw, F., & Horálek, J. (2011). Sub-grid variability and its impact on European wide air quality exposure assessment. *Atmospheric environment*, 45(25), 4220-4229. .

890 Finlayson-Pitts, B. J. and Pitts, J. N., J.: Tropospheric air pollution: Ozone, airborne toxics,  
891 polycyclic aromatic hydrocarbons, and particles, *Science*, 276, 1045–1052, 1997.

892 Fishman, J., Silverman, M. L., Crawford, J. H., and Creilson, J. K.: A study of regional-scale  
893 variability of in situ and model-generated tropospheric trace gases: Insights into observational  
894 requirements for a satellite in geostationary orbit, *Atmos. Environ.*, 45, 4682–4694, 2011.

895 Follette-Cook, M., Pickering, K., Crawford, J., Duncan, B., Loughner, C., Diskin, G., Fried, A.,  
896 and Weinheimer, A.: Spatial and temporal variability of trace gas columns derived from  
897 WRF/Chem regional model output: Planning for geostationary observations of atmospheric  
898 composition, *Atmos. Environ.*, 118, 28–44, doi:10.1016/j.atmosenv.2015.07.024, 2015.

899 Friedl, M., Sulla-Menashe, D. (2015). MCD12C1 MODIS/Terra+Aqua Land Cover Type Yearly  
900 L3 Global 0.05Deg CMG V006 [Data set]. NASA EOSDIS Land Processes DAAC. Accessed  
901 2019-08-12 from <https://doi.org/10.5067/MODIS/MCD12C1.006>.

902 Gaubert, B., Coman, A., Foret, G., Meleux, F., Ung, A., Rouil, L., Ionescu, A., Candau, Y., and  
903 Beekmann, M.: Regional scale ozone data assimilation using an ensemble Kalman filter and the  
904 CHIMERE chemical transport model, *Geosci. Model Dev.*, 7, 283–302,  
905 <https://doi.org/10.5194/gmd-7-283-2014>, 2014.

906 Gaubert, B., Emmons, L. K., Raeder, K., Tilmes, S., Miyazaki, K., Arellano Jr., A. F., Elguindi,  
907 N., Granier, C., Tang, W., Barré, J., Worden, H. M., Buchholz, R. R., Edwards, D. P., Franke, P.,  
908 Anderson, J. L., Saunio, M., Schroeder, J., Woo, J.-H., Simpson, I. J., Blake, D. R., Meinardi, S.,  
909 Wennberg, P. O., Crounse, J., Teng, A., Kim, M., Dickerson, R. R., He, H., Ren, X., Pusede, S. E.,  
910 and Diskin, G. S.: Correcting model biases of CO in East Asia: impact on oxidant distributions  
911 during KORUS-AQ, *Atmos. Chem. Phys.*, 20, 14617–14647, [https://doi.org/10.5194/acp-20-](https://doi.org/10.5194/acp-20-14617-2020)  
912 [14617-2020](https://doi.org/10.5194/acp-20-14617-2020), 2020.

913 Gerbig, C., Lin, J. C., Wofsy, S. C., Daube, B. C., Andrews, A. E., Stephens, B. B., Bakwin, P. S.,  
914 and Grainger, C. A.: Toward constraining regional-scale fluxes of CO<sub>2</sub> with atmospheric  
915 observations over a continent: 1. Observed spatial variability from airborne platforms, *J. Geophys.*  
916 *Res.-Atmos.*, 108, 4756, doi:4710.1029/2002JD003018, 2003.

917 Global Modeling and Assimilation Office (GMAO) (2015), MERRA-2 inst3\_3d\_asm\_Nv: 3d,3-  
918 Hourly,Instantaneous,Model-Level,Assimilation,Assimilated Meteorological Fields V5.12.4,  
919 Greenbelt, MD, USA, Goddard Earth Sciences Data and Information Services Center (GES DISC),  
920 Accessed: Mar 29, 2021, [10.5067/WWQSQXQ8IVFW8](https://doi.org/10.5067/WWQSQXQ8IVFW8).

921 Griffin, D., Zhao, X., McLinden, C. A., Boersma, F., Bourassa, A., Dammers, E., Degenstein, D.,  
922 Eskes, H., Fehr, L., Fioletov, V., Hayden, K., Kharol, S. K., Li, S.-M., Makar, P., Martin, R. V.,  
923 Mihele, C., Mittermeier, R. L., Krotkov, N., Snee, M., Lamsal, L. N., ter Linden, M., van Geffen,  
924 J., Veefkind, P., and Wolde, M.: High-Resolution Mapping of Nitrogen Dioxide with TROPOMI:  
925 First Results and Validation Over the Canadian Oil Sands, *Geophys. Res. Lett.*, 46, 1049–1060,  
926 <https://doi.org/10.1029/2018GL081095>, 2019.

927 Harris, D., Foufoula-Georgiou, E., Droegemeier, K. K., and Levit, J. J.: Multiscale Statistical  
928 Properties of a High-Resolution Precipitation Forecast, *J. Hydrometeor.*, 2, 406–418, 2001.

**Deleted:** Finlayson-Pitts, B. J., & Pitts, J. N. (1997). Tropospheric air pollution: ozone, airborne toxics, polycyclic aromatic hydrocarbons, and particles. *Science*, 276(5315), 1045-1051.

**Deleted:** Fishman, J., Silverman, M. L., Crawford, J. H., & Creilson, J. K. (2011). A study of regional-scale variability of in situ and model-generated tropospheric trace gases: Insights into observational requirements for a satellite in geostationary orbit. *Atmospheric environment*, 45(27), 4682-4694.

**Deleted:** Follette-Cook, M. B., Pickering, K. E., Crawford, J. H., Duncan, B. N., Loughner, C. P., Diskin, G. S., ... & Weinheimer, A. J. (2015). Spatial and temporal variability of trace gas columns derived from WRF/Chem regional model output: Planning for geostationary observations of atmospheric composition. *Atmospheric Environment*, 118, 28-44.

**Deleted:** Gaubert, B., L. K. Emmons, K. Raeder, S. Tilmes, K. Miyazaki, A. F. Arellano Jr, N. Elguindi, C. Granier, W. Tang, J. Barré, H. M. Worden, R. R. Buchholz, D. P. Edwards, P. Franke, J. L. Anderson, M. Saunio, J. Schroeder, J.-H. Woo, I. J. Simpson, D. R. Blake, S. Meinardi, P. O. Wennberg, J. Crounse, A. Teng, M. Kim, R. R. Dickerson, H. He, X. Ren, S. E. Pusede, and G. S. Diskin (2020), Correcting model biases of CO in East Asia: impact on oxidant distributions during KORUS-AQ, *Atmos. Chem. Phys.*, 20, 14617–14647, - <https://doi.org/10.5194/acp-20-14617-2020>.

**Deleted:** -

**Deleted:** Griffin, D., Zhao, X., McLinden, C. A., Boersma, F., Bourassa, A., Dammers, E., ... & Hayden, K. (2019). High-resolution mapping of nitrogen dioxide with TROPOMI: First results and validation over the Canadian oil sands. *Geophysical Research Letters*, 46(2), 1049-1060.

**Deleted:** Harris, D., Foufoula-Georgiou, E., Droegemeier, K. K., Levit, J. J., 2001. Multiscale statistical properties of a high-resolution precipitation forecast. *J. Hydrometeor.* 2, 406-418.

967 Hoesly, R. M., Smith, S. J., Feng, L., Klimont, Z., Janssens-Maenhout, G., Pitkanen, T., Seibert,  
968 J. J., Vu, L., Andres, R. J., Bolt, R. M., Bond, T. C., Dawidowski, L., Kholod, N., Kurokawa, J.-  
969 I., Li, M., Liu, L., Lu, Z., Moura, M. C. P., O'Rourke, P. R., and Zhang, Q.: Historical (1750–2014)  
970 anthropogenic emissions of reactive gases and aerosols from the Community Emissions Data  
971 System (CEDS), *Geosci. Model Dev.*, 11, 369–408, <https://doi.org/10.5194/gmd-11-369-2018>,  
972 2018.

973 Huang, M., Crawford, J. H., Diskin, G. S., Santanello, J. A., Kumar, S. V., Pusede, S. E., Parrington,  
974 M., and Carmichael, G. R.: Modeling Regional Pollution Transport Events During KORUS-AQ:  
975 Progress and Challenges in Improving Representation of Land-Atmosphere Feedbacks, *J. Geophys.*  
976 *Res.-Atmos.*, 123, 10–732, 2018.

977 Janjic, T., Bormann, N., Bocquet, M., Carton, J. A., Cohn, S. E., Dance, S. L., Losa, S. N.,  
978 Nichols, N. K., Potthast, R., Waller, J. A., and Weston, P.: On the representation error in data  
979 assimilation, *Q. J. R. Meteorol. Soc.*, 144, 1257–1278, <https://doi.org/10.1002/qj.3130>, 2018.

980 Judd, L. M., Al-Saadi, J. A., Janz, S. J., Kowalewski, M. G., Pierce, R. B., Szykman, J. J., Valin,  
981 L. C., Swap, R., Cede, A., Mueller, M., Tiefengraber, M., Abuhassan, N., and Williams, D.:  
982 Evaluating the impact of spatial resolution on tropospheric NO<sub>2</sub> column comparisons within urban  
983 areas using high-resolution airborne data, *Atmos. Meas. Tech.*, 12, 6091–6111,  
984 <https://doi.org/10.5194/amt-12-6091-2019>, 2019.

985 Kim, H. C., Lee, P., Judd, L., Pan, L., and Lefer, B.: OMI NO<sub>2</sub> column densities over North  
986 American urban cities: the effect of satellite footprint resolution, *Geosci. Model Dev.*, 9, 1111–  
987 1123, <https://doi.org/10.5194/gmd-9-1111-2016>, 2016.

988 Kim, H., Zhang, Q., and Heo, J.: Influence of intense secondary aerosol formation and long-range  
989 transport on aerosol chemistry and properties in the Seoul Metropolitan Area during spring time:  
990 results from KORUS-AQ, *Atmos. Chem. Phys.*, 18, 7149–7168, [https://doi.org/10.5194/acp-18-](https://doi.org/10.5194/acp-18-7149-2018)  
991 7149-2018, 2018.

992 Kim, J., Jeong, U., Ahn, M.-H., Kim, J. H., Park, R. J., Lee, H., Song, C. H., Choi, Y.-S., Lee, K.-  
993 H., Yoo, J.-M., Jeong, M.-J., Park, S. K., Lee, K.-M., Song, C.-K., Kim, S.-W., Kim, Y. J., Kim,  
994 S.-W., Kim, M., Go, S., Liu, X., Chance, K., Miller, C. C., Al-Saadi, J., Veihelmann, B., Bhartia,  
995 P. K., Torres, O., Abad, G. G., Haffner, D. P., Ko, D. H., Lee, S. H., Woo, J.-H., Chong, H., Park,  
996 S. S., Nicks, D., Choi, W. J., Moon, K.-J., Cho, A., Yoon, J., Kim, S.-K., Hong, H., Lee, K., Lee,  
997 H., Lee, S., Choi, M., Veeckind, P., Levelt, P. F., Edwards, D. P., Kang, M., Eo, M., Bak, J., Baek,  
998 K., Kwon, H.-A., Yang, J., Park, J., Han, K. M., Kim, B.-R., Shin, H.-W., Choi, H., Lee, E., Chong,  
999 J., Cha, Y., Koo, J.-H., Irie, H., Hayashida, S., Kasai, Y., Kanaya, Y., Liu, C., Lin, J., Crawford,  
1000 J. H., Carmichael, G. R., Newchurch, M. J., Lefer, B. L., Herman, J. R., Swap, R. J., Lau, A. K.  
1001 H., Kurosu, T. P., Jaross, G., Ahlers, B., Dobber, M., McElroy, C. T., and Choi, Y.: New era of air  
1002 quality monitoring from space, *Geostationary Environment Monitoring Spectrometer (GEMS), B.*  
1003 *Am. Meteorol. Soc.*, 101, E1–E22, <https://doi.org/10.1175/BAMS-D-18-0013.1>, 2020.

1004 Lamsal, L. N., Janz, S., Krotkov, N., Pickering, K. E., Spurr, R. J. D., Kowalewski, M., Loughner,  
1005 C. P., Crawford, J., Swartz, W. H., and Herman, J. R.: High-resolution NO<sub>2</sub> observations from the

**Deleted:** Huang, M., Crawford, J. H., Diskin, G. S., Santanello, J. A., Kumar, S. V., Pusede, S. E., ... & Carmichael, G. R. (2018). Modeling Regional Pollution Transport Events During KORUS-AQ: Progress and Challenges in Improving Representation of Land-Atmosphere Feedbacks. *Journal of Geophysical Research: Atmospheres*, 123(18), 10-732.

**Deleted:** Kim, H., Zhang, Q., & Heo, J. (2018). Influence of intense secondary aerosol formation and long-range transport on aerosol chemistry and properties in the Seoul Metropolitan Area during spring time: results from KORUS-AQ. *Atmospheric Chemistry and Physics*, 18(10), 7149-7168.

**Deleted:** Kim, J., Jeong, U., Ahn, M. H., Kim, J. H., Park, R. J., Lee, H., ... & Jeong, M. J. (2020). New era of air quality monitoring from space: Geostationary Environment Monitoring Spectrometer (GEMS). *Bulletin of the American Meteorological Society*, (2020), 00. .

1024 [Airborne Compact Atmospheric Mapper: Retrieval and validation, J. Geophys. Res., 122, 1953–](#)  
1025 [1970, https://doi.org/10.1002/2016JD025483, 2017.](#)

1026 Leitch, J. W., Delker, T., Good, W., Ruppert, L., Murcray, F., Chance, K., Liu, X., Nowlan, C.,  
1027 Janz, S. J., Krotkov, N. A., Pickering, K. E., Kowalewski, M., and Wang, J.: The GeoTASO  
1028 airborne spectrometer project, Earth Observing Systems XIX, 17–21 August 2014, San Diego,  
1029 California, United States, Proc. SPIE, 9218, 92181H-9, <https://doi.org/10.1117/12.2063763>, 2014.

1030 Levelt, P. F., Oord, G. H. J. van den, Dobber, M. R., Malkki, A., Visser, H., Vries, J. de, Stammes,  
1031 P., Lundell, J. O. V., and Saari, H.: The ozone monitoring instrument, IEEE T. Geosci. Remote,  
1032 44, 1093–1101, <https://doi.org/10.1109/TGRS.2006.872333>, 2006.

1033 [Levelt, P. F., Joiner, J., Tamminen, J., Veefkind, J. P., Bhartia, P. K., Stein Zweers, D. C., Duncan,](#)  
1034 [B. N., Streets, D. G., Eskes, H., van der A, R., McLinden, C., Fioletov, V., Carn, S., de Laat, J.,](#)  
1035 [DeLand, M., Marchenko, S., McPeters, R., Ziemke, J., Fu, D., Liu, X., Pickering, K., Apituley, A.,](#)  
1036 [González Abad, G., Arola, A., Boersma, F., Chan Miller, C., Chance, K., de Graaf, M.,](#)  
1037 [Hakkorainen, J., Hassinen, S., Jalongo, I., Kleipool, Q., Krotkov, N., Li, C., Lamsal, L., Newman,](#)  
1038 [P., Nowlan, C., Suleiman, R., Tilstra, L. G., Torres, O., Wang, H., and Wargan, K.: The Ozone](#)  
1039 [Monitoring Instrument: overview of 14 years in space, Atmos. Chem. Phys., 18, 5699–5745,](#)  
1040 <https://doi.org/10.5194/acp-18-5699-2018>, 2018.

1041 [Miyazaki, K., Sekiya, T., Fu, D., Bowman, K., Kulawik, S., Sudo, K., Walker, T., Kanaya, Y.,](#)  
1042 [Takigawa, M., Ogochi, K., Eskes, H., Boersma, K. F., Thompson, A. M., Gaubert, B., Barre, J.,](#)  
1043 [and Emmons, L. K.: Balance of Emission and Dynamical Controls on Ozone During the Korea-](#)  
1044 [United States Air Quality Campaign From Multiconstituent Satellite Data Assimilation, J.](#)  
1045 [Geophys. Res.-Atmos., 124, 387–413, 2019.](#)

1046 National Centers for Environmental Prediction/National Weather Service/NOAA/U.S.  
1047 Department of Commerce. 2015, updated daily. NCEP GDAS/FNL 0.25 Degree Global  
1048 Tropospheric Analyses and Forecast Grids. Research Data Archive at the National Center for  
1049 Atmospheric Research, Computational and Information Systems Laboratory.  
1050 <https://doi.org/10.5065/D65Q4T4Z>.

1051 Nowlan, C. R., Liu, X., Leitch, J. W., Chance, K., González Abad, G., Liu, C., Zoogman, P., Cole,  
1052 J., Delker, T., Good, W., Murcray, F., Ruppert, L., Soo, D., Follette-Cook, M. B., Janz, S. J.,  
1053 Kowalewski, M. G., Loughner, C. P., Pickering, K. E., Herman, J. R., Beaver, M. R., Long, R. W.,  
1054 Szykman, J. J., Judd, L. M., Kelley, P., Luke, W. T., Ren, X., and Al-Saadi, J. A.: Nitrogen dioxide  
1055 observations from the Geostationary Trace gas and Aerosol Sensor Optimization (GeoTASO)  
1056 airborne instrument: Retrieval algorithm and measurements during DISCOVER-AQ Texas 2013,  
1057 Atmos. Meas. Tech., 9, 2647–2668, <https://doi.org/10.5194/amt-9-2647-2016>, 2016.

1058 Nowlan, C. R., Liu, X., Janz, S. J., Kowalewski, M. G., Chance, K., Follette-Cook, M. B., Fried,  
1059 A., González Abad, G., Herman, J. R., Judd, L. M., Kwon, H.-A., Loughner, C. P., Pickering, K.  
1060 E., Richter, D., Spinei, E., Walega, J., Weibring, P., and Weinheimer, A. J.: Nitrogen dioxide and  
1061 formaldehyde measurements from the GEOstationary Coastal and Air Pollution Events (GEO-  
1062 CAPE) Airborne Simulator over Houston, Texas, Atmos. Meas. Tech., 11, 5941–5964,  
1063 <https://doi.org/10.5194/amt11-5941-2018>, 2018.

**Deleted:** Lamsal, L.N., Janz, S.J., Krotkov, N.A., Pickering, K.E., Spurr, R.J.D., Kowalewski, M.G., Loughner, C.P., Crawford, J.H., Swartz, W.H., Herman, J.R., 2017. High-resolution NO<sub>2</sub> observations from the airborne Compact atmospheric mapper: retrieval and validation. J. Geophys. Res.: Atmospheres 122 (3), 1953–1970.

**Deleted:** Levelt, P. F., Joiner, J., Tamminen, J., Veefkind, J. P., Bhartia, P. K., & Carn, S. (2018). The Ozone Monitoring Instrument: overview of 14 years in space. Atmospheric Chemistry and Physics, 18, 5699.

**Deleted:** Miyazaki, K., Sekiya, T., Fu, D., Bowman, K. W., Kulawik, S. S., Sudo, K., ... & Eskes, H. (2019). Balance of Emission and Dynamical Controls on Ozone During the Korea-United States Air Quality Campaign From Multiconstituent Satellite Data Assimilation. Journal of Geophysical Research: Atmospheres, 124(1), 387-413.



1080 Pfister, G. G., Eastham, S. D., Arellano, A. F., Aumont, B., Barsanti, K. C., Barth, M. C., Conley,  
 1081 A., Davis, N. A., Emmons, L. K., Fast, J. D., Fiore, A. M., Gaubert, B., Goldhaber, S., Granier, C.,  
 1082 Grell, G. A., Guevara, M., Henze, D. K., Hodzic, A., Liu, X., Marsh, D. R., Orlando, J. J., Plane,  
 1083 J. M. C., Polvani, L. M., Rosenlof, K. H., Steiner, A. L., Jacob, D. J., and Brasseur, G. P.: The  
 1084 Multi-Scale Infrastructure for Chemistry and Aerosols (MUSICA). *B. Am. Meteorol. Soc.*, **101**,  
 1085 1743–1760, 2020.

1086 Pillai, D., Gerbig, C., Marshall, J., Ahmadov, R., Kretschmer, R., Koch, T., and Karstens, U.: High  
 1087 resolution modeling of CO<sub>2</sub> over Europe: implications for representation errors of satellite  
 1088 retrievals, *Atmos. Chem. Phys.*, **10**, 83–94, <https://doi.org/10.5194/acp-10-83-2010>, 2010.

1089 Pinardi, G., Van Roozendaal, M., Hendrick, F., Theys, N., Abuhassan, N., Bais, A., Boersma, F.,  
 1090 Cede, A., Chong, J., Donner, S., Drosoglou, T., Dzhola, A., Eskes, H., Frieß, U., Granville, J.,  
 1091 Herman, J. R., Holla, R., Hovila, J., Irie, H., Kanaya, Y., Karagkiozidis, D., Kouremeti, N.,  
 1092 Lambert, J.-C., Ma, J., Peters, E., Piters, A., Postlyakov, O., Richter, A., Remmers, J., Takashima,  
 1093 H., Tiefengraber, M., Valks, P., Vlemmix, T., Wagner, T., and Wittrock, F.: Validation of  
 1094 tropospheric NO<sub>2</sub> column measurements of GOME-2A and OMI using MAX-DOAS and direct  
 1095 sun network observations, *Atmos. Meas. Tech.*, **13**, 6141–6174, [https://doi.org/10.5194/amt-13-](https://doi.org/10.5194/amt-13-6141-2020)  
 1096 6141-2020, 2020.

1097 Qian, Y., Gustafson Jr., W. I., and Fast, J. D.: An investigation of the sub-grid variability of trace  
 1098 gases and aerosols for global climate modeling, *Atmos. Chem. Phys.*, **10**, 6917–6946,  
 1099 <https://doi.org/10.5194/acp-10-6917-2010>, 2010.

1100 Song, H., Zhang, Z., Ma, P.-L., Ghan, S., and Wang, M.: The importance of considering sub-grid  
 1101 cloud variability when using satellite observations to evaluate the cloud and precipitation  
 1102 simulations in climate models, *Geosci. Model Dev.*, **11**, 3147–3158, [https://doi.org/10.5194/gmd-](https://doi.org/10.5194/gmd-11-3147-2018)  
 1103 11-3147-2018, 2018.

1104 Spinei, E., Whitehill, A., Fried, A., Tiefengraber, M., Knepp, T. N., Herndon, S., Herman, J. R.,  
 1105 Müller, M., Abuhassan, N., Cede, A., Richter, D., Walega, J., Crawford, J., Szykman, J., Valin, L.,  
 1106 Williams, D. J., Long, R., Swap, R. J., Lee, Y., Nowak, N., and Poche, B.: The first evaluation of  
 1107 formaldehyde column observations by improved Pandora spectrometers during the KORUS-AQ  
 1108 field study, *Atmos. Meas. Tech.*, **11**, 4943–4961, <https://doi.org/10.5194/amt-11-4943-2018>, 2018.

1110 Souri, A. H., Nowlan, C. R., Wolfe, G. M., Lamsal, L. N., Chan Miller, C. E., Abad, G. G., Janz,  
 1111 S. J., Fried, A., Blake, D. R., Weinheimer, A. J., Diskin, G. S., Liu, X., and Chance, K.: Revisiting  
 1112 the effectiveness of HCHO/NO<sub>2</sub> ratios for inferring ozone sensitivity to its precursors using high  
 1113 resolution airborne remote sensing observations in a high ozone episode during the KORUS-AQ  
 1114 campaign, *Atmos. Environ.*, **224**, 117341, <https://doi.org/10.1016/j.atmosenv.2020.117341>, 2020.

1115 Tack, F., Merlaud, A., Iordache, M.-D., Pinardi, G., Dimitropoulou, E., Eskes, H., Bomans, B.,  
 1116 Veefkind, P., and Van Roozendaal, M.: Assessment of the TROPOMI tropospheric NO<sub>2</sub> product  
 1117 based on airborne APEX observations, *Atmos. Meas. Tech.*, **14**, 615–646,  
 1118 <https://doi.org/10.5194/amt-14-615-2021>, 2021.

**Deleted:** Pfister, G. G., Eastham, S. D., Arellano, A. F., Aumont, B., Barsanti, K. C., Barth, M. C., ... & Fiore, A. M. (2020). The Multi-Scale Infrastructure for Chemistry and Aerosols (MUSICA). *Bulletin of the American Meteorological Society*, 101(10), E1743-E1760.

**Deleted:** Spinei, E., Whitehill, A., Fried, A., Tiefengraber, M., Knepp, T. N., Herndon, S., ... & Richter, D. (2018). The first evaluation of formaldehyde column observations by improved Pandora spectrometers during the KORUS-AQ field study. *Atmospheric Measurement Techniques*, 11(9), 4943-4961. .

**Deleted:** Souri, A. H., Nowlan, C. R., Wolfe, G. M., Lamsal, L. N., Miller, C. E. C., Abad, G. G., ... & Diskin, G. S. (2020). Revisiting the effectiveness of HCHO/NO<sub>2</sub> ratios for inferring ozone sensitivity to its precursors using high resolution airborne remote sensing observations in a high ozone episode during the KORUS-AQ campaign. *Atmospheric Environment*, 117341. .

[... [2]



1138 Tang, W., Arellano, A. F., DiGangi, J. P., Choi, Y., Diskin, G. S., Agustí-Panareda, A., Parrington,  
 1139 M., Massart, S., Gaubert, B., Lee, Y., Kim, D., Jung, J., Hong, J., Hong, J.-W., Kanaya, Y., Lee,  
 1140 M., Stauffer, R. M., Thompson, A. M., Flynn, J. H., and Woo, J.-H.: Evaluating high-resolution  
 1141 forecasts of atmospheric CO and CO<sub>2</sub> from a global prediction system during KORUS-AQ field  
 1142 campaign, *Atmos. Chem. Phys.*, 18, 11007–11030, <https://doi.org/10.5194/acp-18-11007-2018>,  
 1143 2018.

1144 Tang, W., Emmons, L. K., Arellano Jr., A. F., Gaubert, B., Knote, C., Tilmes, S., Buchholz, R. R.,  
 1145 Pfister, G. G., Diskin, G. S., Blake, D. R., Blake, N. J., Meinardi, S., DiGangi, J. P., Choi, Y., Woo,  
 1146 J.-H., He, C., Schroeder, J. R., Suh, I., Lee, H.-J., Jo, H.-Y., Kanaya, Y., Jung, J., Lee, Y., and Kim,  
 1147 D.: Source contributions to carbon monoxide concentrations during KORUS-AQ based on CAM-  
 1148 chem model applications, J. Geophys. Res.-Atmos., 124, 1–27,  
 1149 <https://doi.org/10.1029/2018jd029151>, 2019.

1150 Tang, W., Worden, H. M., Deeter, M. N., Edwards, D. P., Emmons, L. K., Martínez-Alonso, S.,  
 1151 Gaubert, B., Buchholz, R. R., Diskin, G. S., Dickerson, R. R., Ren, X., He, H., and Kondo, Y.:  
 1152 Assessing Measurements of Pollution in the Troposphere (MOPITT) carbon monoxide retrievals  
 1153 over urban versus non-urban regions, *Atmos. Meas. Tech.*, 13, 1337–1356,  
 1154 <https://doi.org/10.5194/amt-13-1337-2020>, 2020.

1155 Valin, L. C., Russell, A. R., Hudman, R. C., and Cohen, R. C.: Effects of model resolution on the  
 1156 interpretation of satellite NO<sub>2</sub> observations, *Atmos. Chem. Phys.*, 11, 11647–11655,  
 1157 <https://doi.org/10.5194/acp-11-11647-2011>, 2011.

1158 Veeffkind, J. P., Aben, I., McMullan, K., Förster, H., de Vries, J., Otter, G., Claas, J., Eskes, H. J.,  
 1159 de Haan, J. F., Kleipool, Q., van Weele, M., Hasekamp, O., Hoogeveen, R., Landgraf, J., Snel, R.,  
 1160 Tol, P., Ingmann, P., Voors, R., Kruizinga, B., Vink, R., Visser, H., and Levelt, P. F.: TROPOMI  
 1161 on the ESA Sentinel-5 Precursor: A GMES mission for global observations of the atmospheric  
 1162 composition for climate, air quality and ozone layer applications, Remote Sens. Environ., 120, 70–  
 1163 83, doi:10.1016/j.rse.2011.09.027, 2012.

1164 van Geffen, J., Boersma, K. F., Eskes, H., Sneep, M., ter Linden, M., Zara, M., and Veeffkind, J.  
 1165 P.: S5P TROPOMI NO<sub>2</sub> slant column retrieval: method, stability, uncertainties and comparisons  
 1166 with OMI, *Atmos. Meas. Tech.*, 13, 1315–1335, <https://doi.org/10.5194/amt-13-1315-2020>, 2020.

1167 Wiedinmyer, C., Akagi, S. K., Yokelson, R. J., Emmons, L. K., Al-Saadi, J. A., Orlando, J. J., and  
 1168 Soja, A. J.: The Fire INventory from NCAR (FINN): a high resolution global model to estimate  
 1169 the emissions from open burning, Geosci. Model Dev., 4, 625–641, [https://doi.org/10.5194/gmd-](https://doi.org/10.5194/gmd-4-625-2011)  
 1170 4-625-2011, 2011.

1171 Zhang, Z., Song, H., Ma, P.-L., Larson, V. E., Wang, M., Dong, X., and Wang, J.: Subgrid  
 1172 variations of the cloud water and droplet number concentration over the tropical ocean: satellite  
 1173 observations and implications for warm rain simulations in climate models, *Atmos. Chem. Phys.*,  
 1174 19, 1077–1096, <https://doi.org/10.5194/acp-19-1077-2019>, 2019.

1175 Zoogman, P., Liu, X., Suleiman, R., Pennington, W., Flittner, D., Al-Saadi, J., Hilton, B., Nicks,  
 1176 D., Newchurch, M., Carr, J., Janz, S., Andraschko, M., Arola, A., Baker, B., Canova, B., Miller,  
 1177 C. C., Cohen, R., Davis, J., Dussault, M., Edwards, D., Fishman, J., Ghulam, A., Abad, G. G.,

**Deleted:** Tang, W., Emmons, L. K., Arellano Jr., A. F., Gaubert, B., Knote, C., Tilmes, S., ... & Blake, N. J. (2019). Source Contributions to Carbon Monoxide Concentrations During KORUS-AQ Based on CAM-chem Model Applications. *Journal of Geophysical Research: Atmospheres*, 124(5), 2796-2822.

**Deleted:** Veeffkind, J. P., Aben, I., McMullan, K., Förster, H., De Vries, J., Otter, G., ... & Van Weele, M. (2012). TROPOMI on the ESA Sentinel-5 Precursor: A GMES mission for global observations of the atmospheric composition for climate, air quality and ozone layer applications. *Remote Sensing of Environment*, 120, 70-83

**Deleted:** Wiedinmyer, C., Akagi, S. K., Yokelson, R. J., Emmons, L. K., Al-Saadi, J. A., Orlando, J. J., & Soja, A. J. (2011). The Fire INventory from NCAR (FINN): A high resolution global model to estimate the emissions from open burning. *Geoscientific Model Development*, 4(3), 625

1195 Grutter, M., Herman, J., Houck, J., Jacob, D., Joiner, J., Kerridge, B., Kim, J., Krotkov, N., Lamsal,  
1196 L., Li, C., Lindfors, A., Martin, R., McElroy, C., McLinden, C., Natraj, V., Neil, D., Nowlan, C.,  
1197 O'Sullivan, E., Palmer, P., Pierce, R., Pippin, M., Saiz-Lopez, A., Spurr, R., Szykman, J., Torres,  
1198 O., Veefkind, J., Veihermann, B., Wang, H., Wang, J., and Chance, K.: Tropospheric emissions:  
1199 Monitoring of pollution (TEMPO), J. Quant. Spectrosc. Ra., 186, 17–39,  
1200 <https://doi.org/10.1016/j.jqsrt.2016.05.008>, 2017.

Deleted: \*

Deleted: Zoogman, P., Liu, X., Suleiman, R. M., Pennington, W. F., Flittner, D. E., Al-Saadi, J. A., ... & Janz, S. J. (2017). Tropospheric emissions: Monitoring of pollution (TEMPO). Journal of Quantitative Spectroscopy and Radiative Transfer, 186, 17-39.

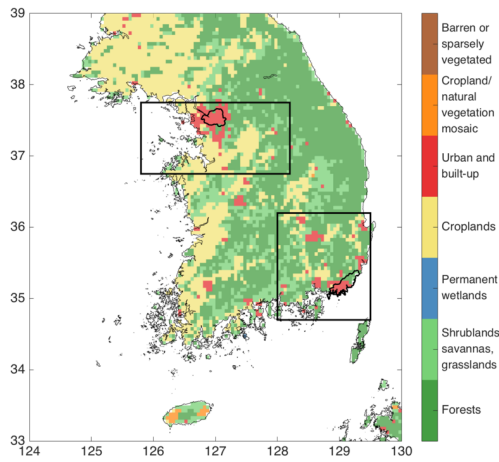
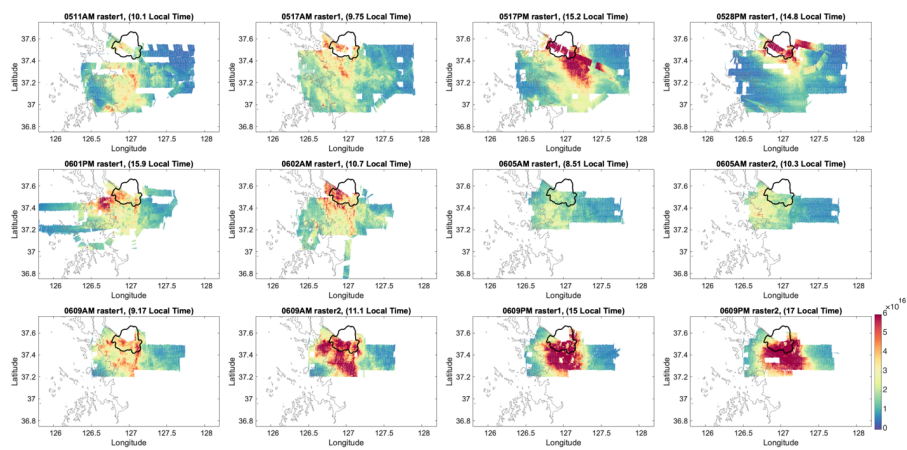


**Figure 1.** Domain of the study over South Korea and the land cover. Boxes indicate location of the SMA (upper left) and the Busan region (lower right) domains. The bold polygons in the two boxes represents political boundaries (upper left) of Seoul and Busan (lower right). Land cover data are from MODIS Terra and Aqua MCD12C1 L3 product, version V006, annual mean at 0.05° resolution; Friedl et al., 2015.



1217  
1218  
1219  
1220  
1221  
1222  
1223  
1224  
1225  
1226  
1227

**Figure 2.** GeoTASO data of tropospheric NO<sub>2</sub> vertical column (molecules cm<sup>-2</sup>) measured during KORUS-AQ over the Seoul region. Each panel shows a separate raster. Panel titles show month, day, AM/PM, raster number on that date, and mean time of raster acquisition. There were nine flights sampling rasters over Seoul. The May 01 AM, May 17 AM, May 17 PM, May 28 PM, June 01 PM, and June 02 AM flights each sampled one raster. The June 05 AM, June 09 AM, and June 09 PM flights each sampled two rasters. As a result, there were two flights and two rasters on May 17th, one flight and two rasters on June 5th, and two flights and four rasters on June 9th. The bold polygons in each panel represent political boundary of Seoul.

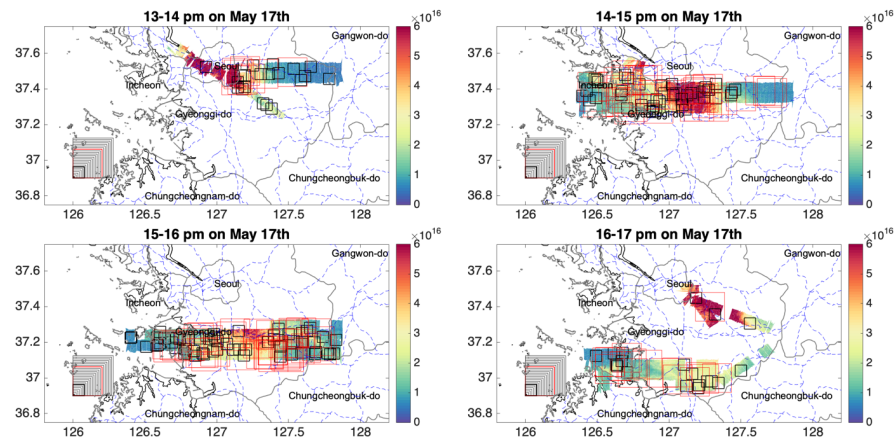
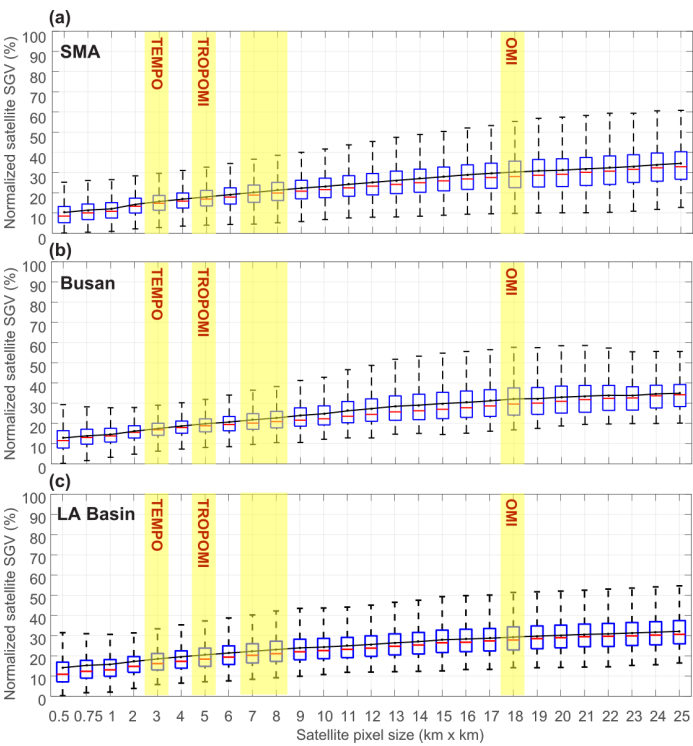


**Figure 3.** Demonstration of the hypothetical satellite pixel random sampling method. Each subplot is an hour during May 17<sup>th</sup> PM flight. For each hour, we randomly sample 10000 hypothetical satellite pixels at each different pixel sizes (i.e., 0.5 km×0.5 km, 0.75 km×0.75 km, 1 km×1 km, 2 km×2 km, ... , 25 km×25 km) over the GeoTASO data of tropospheric NO<sub>2</sub> vertical column (molecules cm<sup>-2</sup>) every hour. The sampled pixel size (from 0.5 km×0.5 km to 25 km×25 km) are shown in the lower-left corner of each sub-plot. Only 100 samples for pixel size of 7 km×7 km (thick black box) and 100 samples for 18 km × 18 km are shown for demonstration purposes. Samples that fail to pass the 75% coverage threshold are not shown. Coastlines, Province/Metropolitan City boundaries are shown by gray solid lines. Main roads are shown by blue dashed lines (data are from <http://www.diva-gis.org/gdata>).



1243  
1244  
1245  
1246  
1247  
1248  
1249  
1250  
1251  
1252  
1253  
1254

**Figure 4.** Boxplot (with medians represented by red bars, interquartile ranges between 25th and 75th percentiles represented by blue boxes, and the most extreme data points not considered outliers represented by whiskers) for the normalized satellite sub-grid variability (SGV) over the Seoul Metropolitan Area (a), the Busan region (b), and Los Angeles Basin (c). Normalized satellite SGV is calculated as the standard deviation of the GeoTASO data within the sampled satellite pixel divided by the mean of the GeoTASO data within the sampled satellite pixel. The black lines represent the mean of the normalized satellite SGV at a given size. The resolutions of TEMPO, TROPOMI, GEMS, and OMI are highlighted by the yellow shade in the Figure.



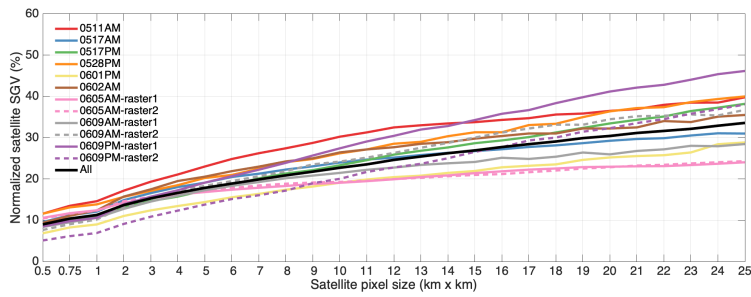
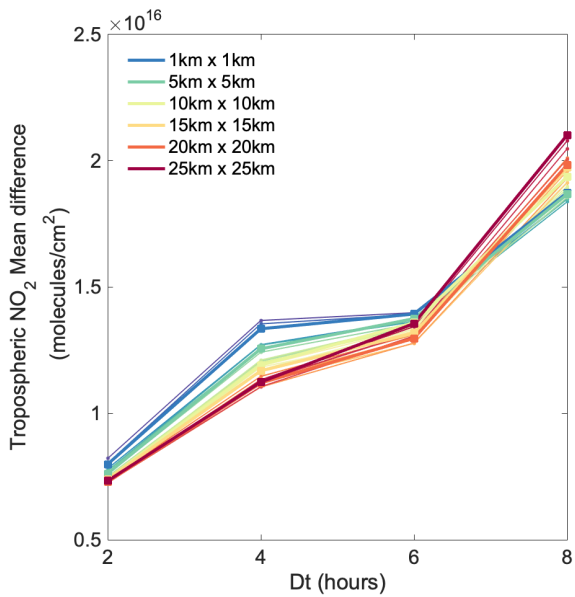


**Figure 5.** Average of the normalized satellite sub-grid variability (SGV) sampled individually from the twelve rasters (represented by the colored lines), and sampled from all the twelve rasters together (represented by the black line) over the Seoul Metropolitan Area during KORUS-AQ. Normalized satellite SGV is calculated by the standard deviation of the GeoTASO data within the sampled satellite pixel divided by the mean of the GeoTASO data within the sampled satellite pixel.



1265  
1266  
1267  
1268  
1269  
1270  
1271  
1272

**Figure 6.** Temporal mean differences (TeMD) of hypothetical satellite pixels (molecules cm<sup>-2</sup>) over the Seoul Metropolitan Area as a function of time difference (Dt). Results for each pixel size are color-coded, with selected sizes shown with thicker lines for reference. See also text for details.

Deleted: retrieved tropospheric NO<sub>2</sub> vertical column

Formatted: Indent: First line: 0", Space Before: 0 pt

Deleted: satellite pixel size

Moved (insertion) [1]

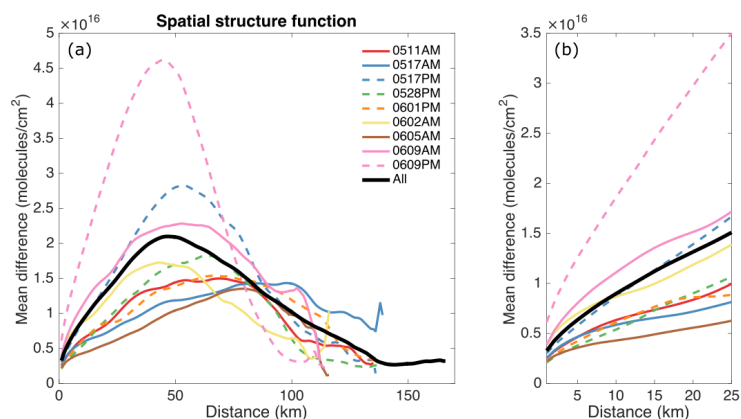
Deleted: (y-axis)

Deleted: .

Deleted: Mean differences for the time difference of Dt are calculated by averaging absolute value of the differences across all sampled satellite pixels that have two values with time difference of Dt.

Moved up [1]: Results for each pixel size are color-coded, with selected sizes shown with thicker lines for reference. .

1283  
1284  
1285



1286  
1287  
1288  
1289  
1290  
1291  
1292  
1293  
1294  
1295  
1296

**Figure 7.** (a) Spatial Structure Function (SSF) for GeoTASO data of tropospheric  $\text{NO}_2$  vertical column molecules  $\text{cm}^{-2}$  over the Seoul Metropolitan Area (SMA) during KORUS-AQ and (b) the zoom-in version of panel (a) for distance range of 1-25 km. The SSF calculates average of absolute value of  $\text{NO}_{2,\text{VC}}$  differences (i.e., mean difference; y-axis) across all data pairs (measured in the same hourly bin) that are separated by different distance (x-axis). The SSF based on GeoTASO data measured during morning flights are in solid colored lines while the SSF based on GeoTASO data measured during afternoon flights are in dashed colored lines. The SSF based on all the data is in the black solid line.

1297  
1298  
1299  
1300  
1301  
1302

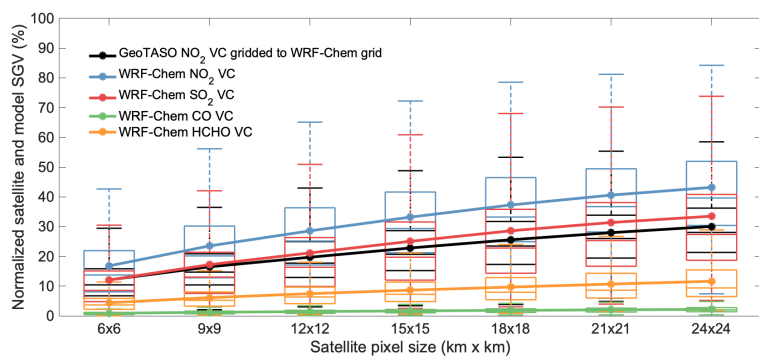


**Figure 8.** Boxplot of hypothetical satellite normalized SGV of NO<sub>2</sub> vertical column (VC), SO<sub>2</sub> VC, CO VC, and formaldehyde (HCHO) VC derived from the WRF-Chem simulation with a resolution of 3 km × 3 km (colored lines), and GeoTASO NO<sub>2</sub> VC that gridded to the WRF-Chem grid (black lines) over the Seoul Metropolitan Area. Medians are represented by red bars, interquartile ranges between 25th and 75th percentiles by blue boxes, and the most extreme data points not considered outliers by whiskers. The modeled NO<sub>2</sub>, CO, SO<sub>2</sub>, and HCHO are filtered to match the rasters of GeoTASO measurements.

In addition to the comparison between different domains and pollution levels, we also compare this relationship in the morning and afternoon. The variation of normalized SGV and pixel size in the morning and afternoon are generally similar for the three regions (Figure S7), except for the large size pixels over SMA, where the normalized SGV is larger in the afternoon than in the morning. This difference is driven by the GeoTASO data from June 9 PM (Figure S4), as the normalized SGV pattern for the afternoon agrees well with the normalized SGV pattern for the morning when the June 9 PM data are excluded. Figure S1 shows that the June 9 PM NO<sub>2</sub> pollution level is higher than other days under meteorological conditions of light winds and moderate temperatures. The MEAN<sub>pixel</sub> values increases ~60% going from 1 km × 1 km to 25 km × 25 km pixel size, while SD<sub>pixel</sub> dramatically increases ~7 times from 1 km × 1 km to 25 km × 25 km. This is higher than any other day, and results in the highest SGV encountered over SMA at the large pixel sizes. We also notice that the normalized SGV does not generally change significantly in the range of 20 km × 20 km to 25 km × 25 km. However, in the case of SMA for June 9 PM, the normalized SGV (as well as SD<sub>pixel</sub>) increases significantly and monotonously with pixel size in the range of 20 km × 20 km to 25 km × 25 km.

Souri, A. H., Nowlan, C. R., Wolfe, G. M., Lamsal, L. N., Miller, C. E. C., Abad, G. G., ... & Diskin, G. S. (2020). Revisiting the effectiveness of HCHO/NO<sub>2</sub> ratios for inferring ozone sensitivity to its precursors using high resolution airborne remote sensing observations in a high ozone episode during the KORUS-AQ campaign. *Atmospheric Environment*, 117341.

Tack, F., Merlaud, A., Iordache, M.-D., Pinardi, G., Dimitropoulou, E., Eskes, H., Bomans, B., Veefkind, P., and Van Roozendaal, M.: Assessment of the TROPOMI tropospheric NO<sub>2</sub> product based on airborne APEX observations, *Atmos. Meas. Tech. Discuss.* [preprint], <https://doi.org/10.5194/amt-2020-148>, in review, 2020.